

Low-ionization structures in planetary nebulae – I: physical, kinematic and excitation properties

Stavros Akras ^{*}, Denise R. Gonçalves

Observatório do Valongo, Universidade Federal do Rio de Janeiro, Ladeira Pedro Antonio 43, 20080-090, Rio de Janeiro, Brazil

Received ****insert****; Accepted ****insert****

ABSTRACT

Though the small-scale, low-ionization knots, filaments and jets (LISs) of planetary nebulae (PNe) are known for ~ 30 yr, some of their observational properties are not well established. In consequence our ability to include them in the wider context of the formation and evolution of PNe is directly affected. Why most structures have lower densities than the PN shells hosting them? Is their intense emission in low-ionization lines the key to their main excitation mechanism? Therefore, if considered altogether, can LISs line ratios, chemical abundances and kinematics enlighten the interplay between the different excitation and formation processes? Here we present a spectroscopic analysis of five PNe that possess LISs confirming that all nebular components have comparable electron temperatures, whereas the electron density is systematically lower in LISs than in the surrounding nebula. Chemical abundances of LISs versus other PN components do not show significant differences as well. By using diagnostic diagrams from shock models, we demonstrate that LISs' main excitation is due to shocks, whereas the other components are mainly photo-ionized. We also propose new diagnostic diagrams involving a few emission lines ($[\text{N II}]$, $[\text{O III}]$, $[\text{S II}]$) and $\log(f_{shocks}/f_{\star})$, where f_{shocks} and f_{\star} are the ionization photon fluxes due to the shocks and the central star ionizing continuum, respectively. A robust relation differentiating the structures is found, with the shock-excited clearly having $\log(f_{shocks}/f_{\star}) > -1$; while the photo-ionized show $\log(f_{shocks}/f_{\star}) < -2$. A transition zone, with $-2 < \log(f_{shocks}/f_{\star}) < -1$ where both mechanisms are equally important, is also defined.

Key words: ISM: abundances – ISM: jets and outflows – ISM: kinematics and dynamics – planetary nebulae: individual: NGC 6572, IC 4846, K 1-2, Wray 1-17, NGC 6891

1 INTRODUCTION

Over the last 30 years, imaging surveys of planetary nebulae (PNe) have brought to light shapes and structures with high complexity (Manchado et al. 1996; Górny et al. 1999; Boumis et al. 2003, 2006; Parker et al. 2006; Sahai 2011; Sabin et al. 2014). Several works have been carried out thus far attempting to group PNe based on their morphologies (Balick 1987; Schwarz et al. 1993; Manchado et al. 1996; Sahai et al. 2011). Any morphological classification of PNe relies on the shape of the large-scale structures (nebular components) such as rims, attached shells and halos, and divide them into five main classes: point-symmetric, elliptical (that includes round), bipolar, multi-polar and irregular. These large-scale structures are better identified in hydrogen recombination lines as well as in bright forbidden O^{++} emission lines.

The formation of spherically symmetric PNe can adequately be explained under the interacting stellar winds model proposed by Kwok et al. (1978). Although, the deviation from spherical symmetry is still an open question (see Balick & Frank 2002; Shaw 2012). A considerable effort has been made to explain the formation of complex PNe morphologies. Most models consider the presence of an equatorial density enhancement in order to collimate the fast stellar wind and result in the formation of the axis-symmetric PNe (e.g. Mellema et al. 1991; Mellema 1995). The former equatorial density enhancement is usually attributed to the mass-exchange interaction between the components in a close binary system (Soker & Livio 1994; Nordhaus & Blackman 2006). Single rotating stars, with or without magnetic fields, have also been investigated as potential origin of the equatorial density enhancement and therefore, the formation of aspherical PNe (García-Segura et al. 1999). Although, very recent magneto-hydrodynamic models have

* e-mail: akras@astro.ufrj.br

shown that complex PNe, such as bipolar, cannot be descendant of single stars (García-Segura et al. 2014).

Another enigmatic and poorly understood component in PNe are the structures on smaller scales than the main nebular components (Balick et al. 1998; Corradi et al. 1996; Gonçalves et al. 2001). These structures are seen mostly in the light of low-ionization lines, such as [N II], [S II], [O II] and [O I]. Corradi et al. (1996) unveiled their presence in various PNe, independently the morphological type, by using the image [N II]/[O III] line ratio technique, which emphasizes the excitation degree through the nebulae.

These small-scale, low-ionization structures (hereafter LISs; Gonçalves et al. 2001) exhibit a variety of morphological types such as knots, jets, jet-like, filaments and head-tails (Balick et al. 1998; Corradi et al. 1996; Gonçalves et al. 2001), whilst they cover a wide range of expansion velocities from few tens to hundreds of km s^{-1} . Based on their expansion velocities, they are labelled as fast, low-ionization emission regions (FLIERs; Balick et al. 1993), bipolar, rotation episodic jets (BRETs; López et al. 1995) or slow moving low ionization emitting regions (SLOWERS; Perinotto 2000). Gonçalves et al. (2001), studying a large number of PNe with LISs, reached the conclusion that LISs appear in all morphological classes of PNe, suggesting that they may not be associated with the mechanisms responsible for the deviation of PNe structures from the spherical symmetry.

Several models have been proposed to explain the formation of LISs, but none of them can provide a general mechanism for all the different types. Jet formation in PNe is usually associated with the interaction of a binary system and an accretion disk around a companion (e.g. Soker & Livio 1994; Blackman et al. 2001). As for the knots, any clue for their formation also needs to consider if they appear in pairs or are randomly distributed (Gonçalves et al. 2001). Symmetric pairs of low-ionization knots seem to appear due to dynamical or/and radiation instabilities (García-Segura et al. 1999). For the isolated knots, *in situ* instabilities Soker & Reveg (1998), and the stagnation knot's model (Steffen et al. 2001) seem to be plausible formation mechanisms that explain some of their characteristics, as much as the shock models from Dopita (1997). For more details on formation mechanisms of LISs see the comprehensive review by Gonçalves et al. (2004). A common characteristic of the models for the formation of LISs is the determination of their age with respect to the main body of the nebula. It has been observationally found that some jets predate the main nebular structure, whereas others appear to be younger, like that of NGC 6337 (Tocknell et al. 2014; Jones et al. 2014) and the jets and knots of the IC 4846, Wray 17-1 and K 1-2 studied in this paper. Altogether the latter two papers quoted, and previous results for the age of LIS in PNe (Gonçalves 2004) reveal a likely connection of LISs with the evolution of the PNe central stars.

Miszalski et al. (2009a) had also proposed a possible link between LISs and the central stars of PNe. These authors argue that LISs seem to be very common in PNe with hydrogen-deficient stars, e.g. [WR]. In this scenario, LISs are likely associated with the turbulence of the strong stellar winds from these, though this connection is still lacking further confirmation. In addition, the same authors claim that there may also exist a relation between the presence of LISs

and the binarity of the central stars, with 40% of post common envelope (CE) PN possessing LISs.

The physical and chemical properties e.g. electron temperature (T_e), electron density (N_e), ionic and elemental abundances of LISs have also been studied by different groups over the past decades (Balick et al. 1993, 1998; Hajian et al. 1997; Gonçalves et al. 2003, 2004, 2009; Leal-Ferreira et al. 2011; Monteiro et al. 2013). No significant difference between the T_e of LISs and that of the higher excitation nebular component (e.g. core, rims, shells) has been found, contrary to the N_e , which is found to be systematically lower in LISs when compared to the surrounding medium. This result is in conflict with the theoretical predictions from the formation models of LISs, which predict LISs to have several times higher density than the surrounding ionized medium. Gonçalves et al. (2009) claim that the mass of LISs must be mostly neutral in order to overcome the discrepancy between models and observations, since all the formation models of LISs calculate the total density of gas (dust, atomic and molecular) and not the electron density, which corresponds only to the ionized fraction of the gas.

The strong [N II] emission line found in LISs compared to the surrounding ionized nebula was firstly attributed to a significant local overabundance of nitrogen (Balick et al. 1994). Mellema et al. (1998) and, more recently, Gonçalves et al. (2006) reached the conclusion that an overabundance of N is not a necessary condition for getting such a strong line-emission. Based on photo-ionization models, Gonçalves et al. (2006) found that the $N^+/N = O^+/O$ assumption of the ionization correction factor (ICF, Kingsburgh & Barlow 1994) should be wrong, and resulting in seemingly overabundance of N in LISs.

Accordingly to the theoretical work by Aleman & Gruenewald (2011), the peak intensity of the low-ionization optical lines ([O II], [N II], [S II], [N I] and [O I]), as well as the H₂ co-rotational lines, occurs in the same narrow transition zone between the ionized and neutral (photo-dissociation) regions. Given that molecular hydrogen can be excited either by shocks or by absorbing UV-photons emitted from the central star, the enhancement of low-ionization lines in LISs may be attributed to these mechanisms. Raga et al. (2008) show that shock models with low and moderate photo-ionization rates are able to reproduce emission line ratios typical of shock-excitation regions, whereas those models with high photo-ionization rates result in emission line ratios similar to photo-ionized nebulae. Therefore, besides the expansion velocities, the evolutionary stage (e.g. the age) and the photo-ionization rate (or the strength) of the central star are crucial parameters in order to distinguish between predominantly shock- and photo-excited structures.

In this series of papers, new spectroscopic data from a sample of 10 PNe that possess LISs are combined with kinematic data in order to study, at the same time, the physico-chemical and morpho-kinematic properties of LISs and other nebular components. The first 5 PNe, with LISs embedded in the main nebular shells, are presented here. The remaining PNe will appear in a forthcoming publication. The observations and data analysis are described in Section 2. The emission line fluxes, the physico-chemical properties, and the morpho-kinematic characteristics of the PNe themselves, as well as of their LISs, are presented in Section 3 and 4, re-

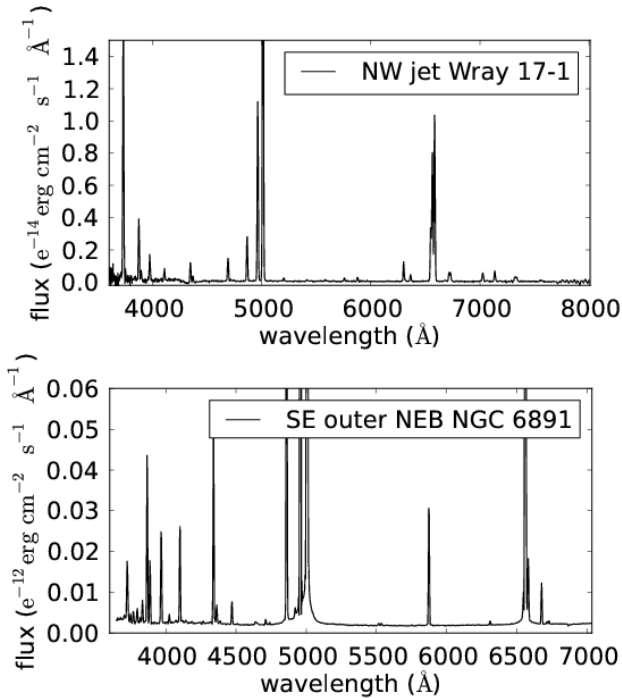


Figure 1. Observed spectra of the NW jet in Wray 17-1 (upper panel), covering the wavelength range of 3600–8000 Å, obtained with DFOSC@Danish, and SE outer NEB in NGC 6891 (lower panel) with a wavelength range of 3650–7050 Å, and observed with the IDS attached to the Isaac Newton telescope.

spectively. The results of this work are discussed in Section 5, and we wrap up with the conclusions in Section 6.

2 OBSERVATIONS

2.1 Intermediate-dispersion Spectroscopy

Intermediate-dispersion spectra of three PNe (NGC 6891 and NGC 6572, IC 4846) were obtained with the 2.5 m Isaac Newton Telescope (INT) at the Observatorio del Roque de los Muchachos, Spain, on 2001 August 30, 31 and September 4, respectively. The Intermediate Dispersion Spectrograph (IDS) was used with the 235 mm camera and the R300V grating resulting in a scale of $3.3 \text{ \AA pixel}^{-1}$ and covering the wavelengths range of 3650–7000 Å. The spatial scale of the instrument was $0.70 \text{ arcsec pixel}^{-1}$, with the TEK5 CCD. The slit width was 1.5 arcsec and the slit length 4 arcmin.

The spectra of K 1-2 and Wray 17-1 were obtained with the 1.54 m Danish telescope at the European Southern Observatory (ESO), La Silla (Chile), on 1997 April 10 and 11, respectively. The Danish Faint Object Spectrograph and Camera (DFOSC) was used with the 2000×2000 CD ($15 \mu\text{m pixel}$) and the Grism #4 ($300 \text{ lines mm}^{-1}$), resulting in $2.2 \text{ \AA pixel}^{-1}$, from 3600 to 8000 Å. The spatial scale of the instrument was $0.40 \text{ arcsec pixel}^{-1}$. The slit width and length were 1.0 arcsec and $>13.7 \text{ arcmin}$, respectively.

Spectro-photometric standard stars were also observed with the INT and Danish telescopes, in order to calibrate the spectra, while the fluxes were corrected for the atmospheric extinction and interstellar reddening. During the night, bias frames, twilight and tungsten flat-field exposures, and wave-

length calibrations were also obtained. Data reduction was performed using the standard IRAF instructions for long-slit spectra. Individual images were bias subtracted and flat-field corrected using a series of twilight flat frames. Two examples of the spectra under analysis, one for each telescope configuration, are presented below in Fig. 1.

2.2 High-dispersion Spectroscopy

High-dispersion, long-slit spectroscopy in the $\text{H}\alpha$ + $[\text{N II}]$ and/or $[\text{O III}]$ emission lines, for 4 out of the 5 PNe in our sample, were acquired from the SPM Kinematic Catalogue of Galactic Planetary Nebulae (López et al. 2012; hereafter KCGPN). The spectra of three PNe (NGC 6572, NGC 6891 and K 1-2) were obtained at the 2.1-m, $f/7.5$ telescope in San Pedro Mártir National Observatory (Mexico), whereas for Wray 17-1, the data were obtained from the 3.9-m, $f/8$ Anglo-Australian telescope in the Siding Spring Observatory (Australia), and in both cases by using the Manchester Echelle Spectrometer (MES-SPM; Meaburn et al. 2003). Two slit widths of 70 and $150 \mu\text{m}$ were used, corresponding to a velocity resolution of 9.2 and 11.5 km s^{-1} , respectively. Additional kinematic information were also drawn for the literature.

3 RESULTS: PHYSICO-CHEMICAL PROPERTIES

In the even numbered tables, from Table 2 to 16, we list the emission line fluxes, corrected for atmospheric extinction and interstellar reddening, for several nebular components, e.g. LISs (knots, jets, filaments), inner and outer main nebular regions (NEB) and for the entire PN, whenever possible. All fluxes are normalized to $F(\text{H}\beta)=100$. The interstellar extinction $c(\text{H}\beta)$ was derived from the Balmer $\text{H}\alpha/\text{H}\beta$ ratio (eq. 1), using the interstellar extinction law by Fitzpatrick (1999) and $R_v=3.1$,

$$c(\text{H}\beta) = \frac{1}{0.348} \log \frac{F(\text{H}\alpha)/F(\text{H}\beta)}{2.85} \quad (1)$$

where 0.348 is the relative logarithmic extinction coefficient for $\text{H}\beta/\text{H}\alpha$.

T_e and N_e for each nebular component were derived by using the TEMDEN task in IRAF (Shaw & Dufour 1995) and are presented in the lowermost part of the flux tables. Given that the abundances derived from collisionally excited lines are strongly dependent on T_e , two combinations of T_e and N_e have been used depending on the degree of ionization of each ion, whenever possible. The combination of $T_e[\text{N II}]$ and $N_e[\text{S II}]$ covers the low-excitation regions (N^+ , O^+ and S^+), whereas the combination of $T_e[\text{O III}]$ and $N_e[\text{S II}]$ covers the medium-excitation regions of these PNe (e.g. O^{++} , S^{++} , Ne^{3+}). Significant differences between the two diagnostic temperatures are found in IC 4846, K 1-2 and NGC 6572, which make the usage of the two diagnostic temperatures necessary for properly deriving the ionic and chemical abundances.

In addition, for a proper estimation of N_e from the $[\text{Ar IV}]$ diagnostic lines, we calculated and subtracted the contribution of the He I $\lambda 4712$ recombination line and those

of the [Ne IV] $\lambda\lambda 4724, 4726$ emission lines to the [Ar IV] $\lambda 4711$ one. In particular, the contribution of the He I $\lambda 4712$ line was calculated using the theoretical work by Benjamin et al. (1999), whereas the contribution of the [Ne IV] $\lambda\lambda 4724, 4726$ emission lines were considered negligible in all cases, given that the central stars of the PNe in this work are not hot enough to ionize Ne^{3+} (P.I.=97.11 eV), except the central star of Wray 17-1 ($T_{\text{eff}}=140000$ K; Rauch and Werner 1997). Although, the N_e of this nebula is extremely low, close to the lower limit, and small changes in the [Ar IV] 4711/4741 line ratio due to the contribution of the [Ne IV] lines will not have a significant impact in the N_e . In short, a comparison of N_e derived from the different diagnostics lines does not show significant differences that could be associated with the [Ne IV] lines. We have to mention here the extreme case of NGC 6891, for which we find significantly higher $N_e[\text{Ar IV}]$, compared to $N_e[\text{S II}]$ and $N_e[\text{Cl III}]$, by factors of 6 and 3.5, respectively. This probably indicates strong density stratification, with denser inner regions with respect to the outer ones.

3.1 IC 4846

IC 4846 (PN G027.6-09.6) is a relatively compact nebula with a size of 10 arcsec. Low angular resolution images of this nebula (Miranda et al. 2001) show two ellipsoidal shells at PAs of 11° (inner shell) and 54° (outer shell). These authors also show the [N II]/ $\text{H}\alpha$ line ratio image which reveals the presence of features enhanced in N^+ : i) a pair of knots, attached to the inner shell, at $\text{PA}=11^\circ$; and ii) a pair of filaments, attached to the outer shell, at $\text{PA}=54^\circ$.

A higher resolution $\text{H}\alpha$ image of IC 4846 (Fig. 2), obtained with the HST in 2001 (program ID:8345; PI: Sahai), clarifies that the pair of filaments is made of highly collimated structures (jets) with some indications of precession. In this new image, the pair of knots along $\text{PA}=11^\circ$ appears to be the result of the interaction between the inner and outer shell. It is worth mentioning here the astonishing similarity between IC 4846 and Fleming 1 (Boffin et al. 2012). Both PNe exhibit a pair of knotty, precessing, bipolar jets or BRETS (López et al. 1995), likely associated with an accretion disk around a binary system. This binary system has already been confirmed in Fleming 1 (Boffin et al. 2012) but not yet in IC 4846.

Nevertheless, the central star of IC 4846 has been classified as a weak emission line or WEL-type star (Acker et al. 1992; Górny et al. 2009). The typical line features of WELs and/or [WC] stars, such as the $\lambda 4650$ (C III–C IV) and the $\lambda 5805$ (C IV) lines, were detected in our spectra with a full width at half maximum (FWHM) of 22 ± 2 and 24 ± 2 Å, respectively. These detections, therefore, reinforce the possibility the central star of IC 4846 may belong to the rare group of binary systems with a WR or WEL-type companion.

In Table 2 we list the emission line fluxes of the inner shell, the pair of jets at $\text{PA}=54^\circ$, and the integrated emission of the nebula along the slit (entire nebula). Unfortunately, no spectra along $\text{PA}=15^\circ$ were obtained. The exact location of the extracted portions of the spectra are shown, and labelled, in Fig. 2.

IC 4846's interstellar extinction, $c(\text{H}\beta)$, is found to vary between 0.48 ± 0.03 and 0.53 ± 0.05 , in excellent agreement

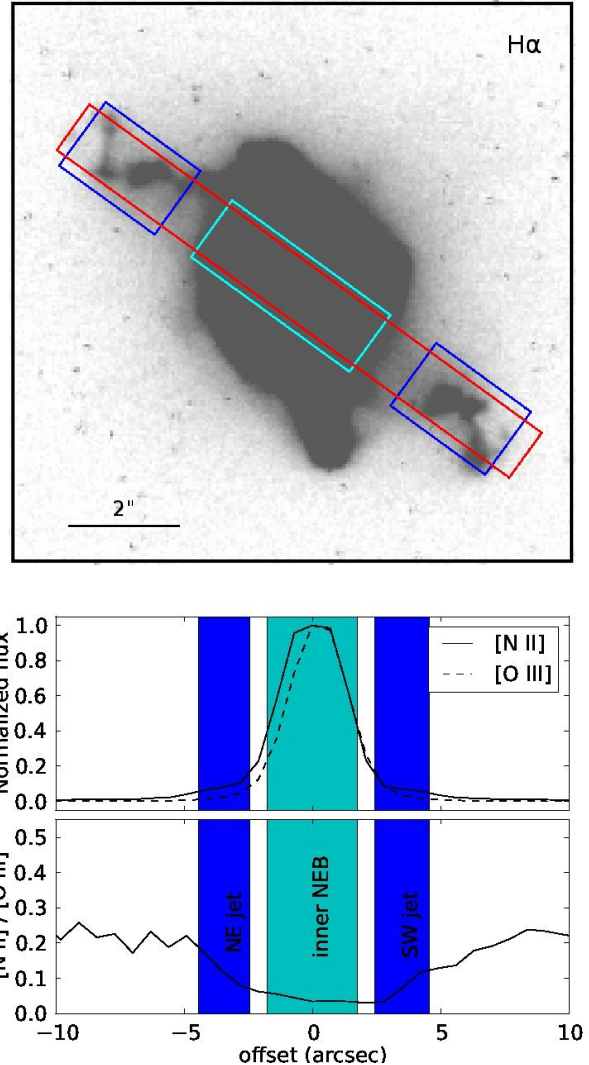


Figure 2. Upper panel: The HST $\text{H}\alpha$ image of IC 4846. The size of the field shown is 10×10 arcsec². The nebular components under analysis are indicated in the image. The extraction windows for these components are indicated by the corresponding boxes: the entire nebula (entire NEB: 10 arcsec, in red), the inner nebula (inner NEB: 3.5 arcsec, in cyan) and the NE and SW jets (2.1 arcsec, in blue). North is up, and East to the left. Lower panels: The radial profile of the [N II] and [O III] emission-line fluxes, normalized to 1.0 and the [N II]/[O III] line ratio, along the slit.

with those derived from previous studies (0.47, Kaler 1986; 0.50, Cahn et al. 1992). Notice, however, that the most recently published value, by Wesson et al. (2005), is higher by a factor of 1.45. One possible explanation for this discrepancy may be the different slit positions ($\text{PA}=0^\circ$ in Wesson et al. 2005). The logarithmic $\text{H}\beta$ fluxes are calculated equal to -11.62, -13.49 and -13.45 and 11.54 for the inner shell, NE jet, SW jet, and the entire nebula, respectively. Acker et al. (1991) give two $\text{H}\beta$ fluxes for this nebula (-11.56 and -11.26), which were derived from the Haute-Provence Observatory spectroscopic data (OHP-CCD) with a slit width of 2.5 arcsec, and from the ESO-CCD, spectra with a slit width of 4 arcsec, respectively. Our value for the entire nebula bet-

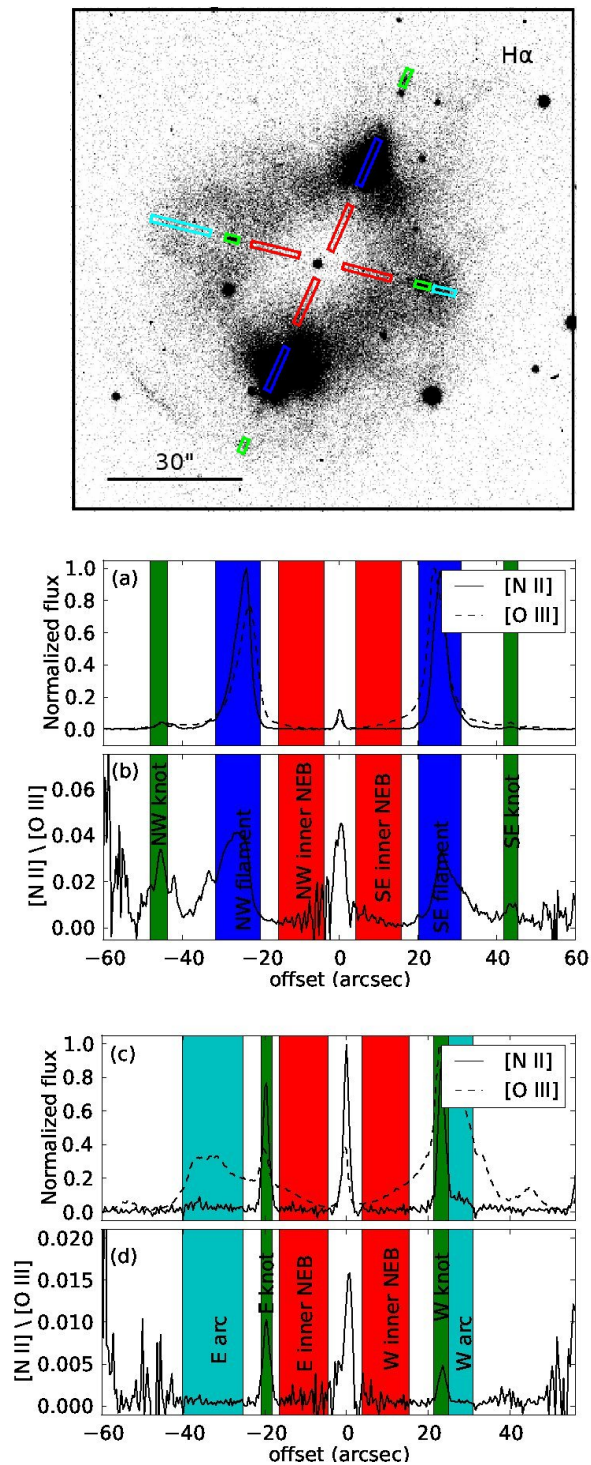


Figure 3. Upper panel: $H\alpha$ image of Wray 17-1 obtained from the ESO Archive. The field shown is 110×110 arcsec². The nebular components under analysis are indicated in the image. The extraction windows for these components are indicated by the corresponding boxes: the inner nebular regions (inner NEB: 11.6 arcsec, in red); the NW and SE blobs (11.6 arcsec and 10.8 arcsec, in blue); the knots (NW knot of 4.4 arcsec, SE knot of 3.6 arcsec, NE knot of 2.8 arcsec, and SW knot of 3.6 arcsec, in green); and the arcs (E arc of 14.8 arcsec and W arc of 6 arcsec, in cyan). North is up, and East is to the left. Lower panels: The radial profile of the $[N II]$ and $[O III]$ emission-line fluxes, normalized to 1.0 and the $[N II]/[O III]$ line ratio along the slits. Panels (a) and (b) correspond to PA=155°, whereas (c) and (d) to PA=75°.

ter agrees with the value derived from the OHP-CCD data because of the same slit widths.

The lower panels in Fig. 2 show the fluxes, normalized to 1.0, of the $[N II]$ (solid-line) and $[O III]$ (dashed-line) emission lines along the slit (panel a), as well as the $[N II]/[O III]$ line ratio (panel b). The (spatial) line profiles and the ratio of these two lines are important in order to better define the sizes of each structure along the slit. The size of each nebular component is indicated in the figures by the coloured regions.

N_e and T_e of IC 4846 are estimated using the diagnostic line ratios of sulfur, argon, chlorine and oxygen. No significant difference is found among them (see Table 2). The comparison of N_e and T_e between the nebular components shows that the jets are significantly less dense than the inner shells, by a factor of 4, whereas, within the errors, all structures have the same T_e . Our N_e values are slightly higher than those found by Wang et al. (2004). We have to notice here that an extremely high $N_e[S II]$ of ~ 20000 cm⁻³ has been reported by Wesson et al. (2005), which is not confirmed by our analysis, neither for the jets nor for the inner shell. Our analysis reveals that the jets in IC 4846 have low N_e , with respect to the main nebular component (inner NEB), and therefore effaces any argument that the LISs in this nebula could have N_e higher than the surrounding medium. The questionable line ratios given by Wesson et al. (2005) were also previously mentioned by Delgado-Inglada et al. (2015).

In Table 3 we present the ionic abundances (obtained using the IONIC task in IRAF; Shaw & Dufour 1995) as well as the total chemical abundances of IC 4846 for each nebular component. The total ones were computed using the ionization correction factor (ICF) from Kingsburgh & Barlow (1994). These authors do not provide an ICF for Cl, thus we used the equation by given Liu et al. (2000).

The low He abundance and N/O ratio of IC 4846 indicate a non-type I nebula. We do not find any trend in chemical abundances among the nebular component; therefore, they are all constant within the uncertainties. A comparison between our total chemical abundances and those found in the literature show a good agreement within the errors, except for Ar (Perinotto et al. 2004; Wesson et al. 2005). The low N abundance in the SW jet is highly uncertain due to the ICF scheme for N (mentioned in the Introduction), as well as to the fact that only N^+ was measured in the different regions. However, both N/H of the SW and NE jet agree, within the errors.

3.2 Wray 17-1

Wray 17-1, or PN G258.0-15.7, displays a diffuse complex nebula of approximately 80 arcsec in diameter (Fig. 3). A pair of bright regions is seen in the $[O III]$, $[N II]$ and $[S II]$ emission line images embedded in the diffuse nebula, along PA=155°. The $[N II]/[O III]$ line ratio image of the nebula unveils highly collimated jet-like structures (Corradi et al. 1999). At the end of these jet-like structures (hereafter filaments), a pair of knots can also be discerned, whereas a second pair of knots is also apparent along the PA=75°. The latter is found to be surrounded by two much fainter arc-like structures. These arcs show an enhanced $[O III]/H\alpha$ ratio, suggesting a shock interaction (Guerrero et al. 2013).

The central star of Wray 17-1 has been found to be a H-

deficient P Cygni star with a $T_{\text{eff}}=140000$ K and $\log(g)=6.3$ (Rauch & Werner 1997). The formation of jets and/or knots may be associated with the strong turbulent stellar winds from this star (Miszalski et al. 2009b) or a putative accretion disk around a close binary system (Soker & Livio 1994, Miszalski et al. 2009b).

Several nebular regions/components are selected for the analysis of this nebula: the pair of filaments, the two pairs of knots, the two arcs and four inner nebular regions, for direct comparison with the properties of the entire nebula. In Fig. 3, we label each of these features with the spatial regions under analysis. The lower panels show the line profiles of the normalized fluxes of the [N II] and [O III] emission lines, as well as their ratio. The position of the filaments and knots is noticeable in these diagrams. The emission line fluxes, the absolute flux of $H\beta$, $c(H\beta)$, N_e and T_e for all these regions are presented in Tables 4 (PA=155°) and 6 (PA=75°). The $c(H\beta)$ of this nebula varies from 0.04 to 0.13 among the nebular component. The average value is 0.08 ± 0.03 , which is in a good agreement with the value derived by Tylenda et al. (1992). $T_e[\text{O III}]$ and $T_e[\text{N II}]$ are found to vary from 11100 K to 14700 K and from 11625 K to 13625 K, respectively. Within the uncertainties, all these measurements agree with one another.

Unlike the T_e , where no variation among the nebular components is found, N_e may show some variation. In particular, the LISs (knots and jet) have higher N_e compared to the inner nebular regions, but because of their high uncertainties, we can say whether the LISs are, in general, less or more dense than the inner nebular regions. Moreover, the N_e values of the inner nebular regions are close to the low density limit of 100 cm^{-3} , and they should be taken with caution.

We present here the first measurements of the ionic and total chemical abundances of Wray 17-1 (Tables 5 and 7). Surprisingly, the knots of Wray 17-1 do not present any He^+ (all He is doubly ionized) and hence the abundance of He cannot be calculated properly, similarly to K 1-2 (see below). The high effective temperature of the central star ($T_{\text{eff}}=140000$ K) is consistent with the high excitation of the nebula. Unlike the knots, the filaments in Wray 17-1 appear to have much lower excitation, where He^+ is more abundant than He^{++} .

3.3 K 1-2

K 1-2 is an elliptical nebula with very low surface brightness and a known binary system. Highly collimated structures with several knots on opposite directions of the central star and a jet-like structure oriented at PA=153° can easily be discerned in the [N II] and [S II], as well as the [O III] and hydrogen recombination line images (Corradi et al. 1999). These authors also found several other knots almost perpendicular to the direction of the jet-like structure, similar to the case of Wray 17-1. The post-CE close binary system found at the centre of K 1-2 would be more easily consistent with the presence of the collimated jet-like structures and knots, as argued in the theoretical works from Soker and Livio (1994), a number of other later works, and the recent observational works by Tocknell et al. (2014) and Jones et al. (2014).

Our spectroscopic data of K 1-2 were obtained only

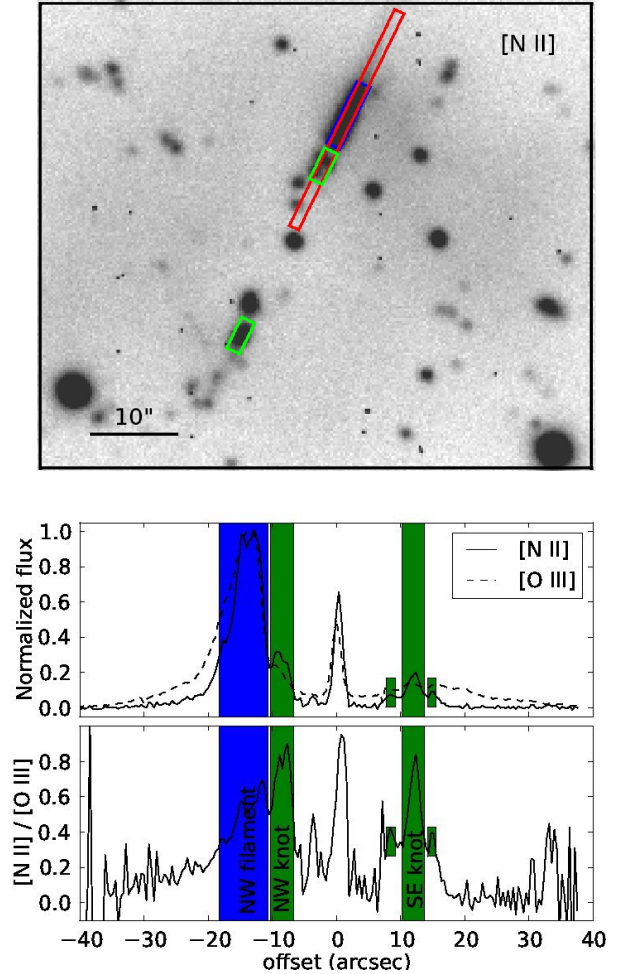


Figure 4. Upper panel: [N II] image of K 1-2 obtained from the ESO archive. The size of the field shown is $62\times 53 \text{ arcsec}^2$. The nebular components under analysis are indicated in the image. The extraction windows for these components are indicated by the corresponding boxes: the Northwest nebula (NW NEB: 35.6 arcsec, in red), the NW filament (7.6 arcsec, in blue) and the knots (NW and SE knots: 3.6 arcsec, in green). North is up, and East is to the left. Lower panels: The radial profile of the [N II] and [O III] emission-line fluxes, normalized to 1.0, and the [N II]/[O III] line ratio, along the slit.

along the PA=153° with the results presented in Table 8. The nebular regions under analysis in this nebula are shown in Fig. 4. We calculate $c(H\beta)$ between 0.22 ± 0.06 and 0.26 ± 0.06 for the various nebular components (NW jet, NW knot and SE knot), which are close to the value derived by Exter et al. (2003) for both north and south jets, namely 0.25. It is worth mentioning here that the $c(H\beta)$ of the entire nebula has been estimated to be 0.11 (Exter et al. 2003), which suggests that the jet and knots are dusty features, at least much more than the surrounding nebula.

The absolute $H\beta$ fluxes for each nebular component are also given in Table 8. For the NW NEB component, the $F(H\beta)$ is $11.4 \times 10^{-15} \text{ ergs s}^{-1} \text{ cm}^{-2}$, which is in very good agreement with the value of the northern jet derived by Exter et al. (2003). We also confirm that $T_e[\text{O III}]$ is ~ 5000 K higher than $T_e[\text{N II}]$, as previously found, but our values are 2000 K and 1000 K, respectively, lower than those in Exter

et al. (2003). N_e is found to vary between $422 \pm 110 \text{ cm}^{-3}$ and $888 \pm 195 \text{ cm}^{-3}$ and, due to the large uncertainties, no unambiguous evidence of variation in N_e between the LISs and nebulae can be provided.

The lower panels of Fig. 4 displays the radial profiles of the [N II] and [O III] emission-line normalized fluxes, as well as the [N II]/[O III] line ratio, along the slit. The exact position of the knots can easily be discerned. Moreover, one can also see that the NW jet is a separate component from the NW knot. The [N II]/[O III] is found to be very high at the position of the knot, close to 0.8, and decreases outwards. The positions of two knots (small green regions) with offsets of 8 and 14 arcsec, respectively, are barely seen in the [N II] line, but they are further away with a sharp peak in the [N II]/[O III] line ratio. These two knots have been noticed by Corradi et al. (1999).

Our NW NEB is the same region studied by Exter et al. (2003), and the chemical abundances are found to be in a good agreement, in the two works. NW NEB has high $\text{He}^{++}/\text{H}^+$ and low O^+/O^{++} ionic abundance ratios indicating a high excitation nebula. Surprisingly, both knots, NW and SE, do not show He^+ lines. Moreover, the high excitation He^{++} and S^{+++} ions are found to be more abundant in these components. Why these knots are so highly excited is an open question. A possible explanation is that the contribution of the main nebula in these components is significant, especially in high-ionization lines (Exter et al. 2003).

3.4 NGC 6891

NGC 6891 (PN G054.1-12.1) displays a bright inner prolate elliptical shell with the major axis oriented along $\text{PA}=135^\circ$, and an inclination angle of $50\text{--}55^\circ$, surrounded by a diffuse spherically symmetric nebula (Guerrero et al. 2000; Palen et al. 2002). Guerrero et al. (2000) pointed out the presence of a (collimated) outflow between the inner and outer nebulae, as well as a pair of faint knots at the tip of these outflows, due to the interaction with the outer nebula (see Fig. 1 from Guerrero et al. 2000). However, HST images of this nebula do not reveal the presence of any collimated outflow (Fig. 5). From our analysis, we found these regions as normal outer nebular regions (outer NEB), instead of LISs.

The central star of NGC 6891 has been classified as an O-type star (McCarthy et al. 1990; Guerrero & De Marco 2013) and as a WEL star (weak emission line, Tylenda et al. 1993). The strong P Cygni profile found in its spectrum implies a terminal velocity of $1200\text{--}1400 \text{ km s}^{-1}$ (Marcolino et al. 2007). Neither the P Cygni nor any wind variability have been detected in the central star spectrum, by Guerrero & De Marco (2013). Nevertheless, the detection in its spectrum of the $\lambda 4650$ (C III 4647/51 and C IV 4658) and $\lambda 5805$ (C IV 5801–5812) line features, in conjunction with the absence of the emission line C III $\lambda 5696$ line, support the WEL-type classification. The He II $\lambda\lambda 4541, 5412$ absorption lines, previously reported by Parthasarathy et al. (1998) and Marcolino & de Araújo (2003), were also detected by us.

Two spectra were obtained for this nebula, with the slits positioned along $\text{PA } 45^\circ$ and 135° . The identification of all nebular components used for the analysis is given in Fig. 5. The logarithmic $F(\text{H}\beta)$ flux derived for the entire NEB are -11.29 and -11.31 for the $\text{PA}=135^\circ$ and $\text{PA}=45^\circ$, respectively, in good agreement with those from Acker et

al. (1991) work. $c(\text{H}\beta)$ is calculated between 0.03 ± 0.02 and 0.06 ± 0.04 (for the different nebular components). Be aware that, our values are substantially lower than those derived by Kaler et al. (1970) and Wesson et al. (2005), namely 0.41 and 0.29, respectively. The different slit positions between the aforementioned studies and ours may cause this discrepancy in $c(\text{H}\beta)$.

$T_e[\text{O III}]$ of the entire nebula, for both PAs, are $9600 \pm 1630 \text{ K}$ and $9500 \pm 1420 \text{ K}$, whereas $T_e[\text{N II}]$ is found to be higher by $\sim 3000 \text{ K}$ (12720 ± 6360 and $12190 \pm 5900 \text{ K}$). These value agree with the previously published ones: $T_e[\text{O III}]=9200 \text{ K}$ and $T_e[\text{N II}]=10600 \text{ K}$ (Henry et al. 2004) and $T_e[\text{O III}]=9330 \text{ K}$ (Wesson et al. 2005). As for the N_e , we derive $N_e[\text{S II}]=1290 \pm 390 \text{ cm}^{-3}$, $N_e[\text{Cl III}]=2460 \pm 490 \text{ cm}^{-3}$, and $N_e[\text{Ar IV}]=2508 \pm 640 \text{ cm}^{-3}$, which also agree within the errors with those densities derived by Wesson et al. (2005). The high N_e value of 10000 cm^{-3} , reported by Henry et al. (2004), is not confirmed in this work, nor in any other so far available in the literature (Kaler 1970; Wesson et al. 2005).

A comparison of T_e and N_e among the inner NEB, outer NEB, and knots, do not reveal any important difference. The surprisingly high $N_e[\text{Ar IV}]$ found in the inner NEB, may be indicating a density stratification in the inner core.

Recent [N II] and [O III] HST images of NGC 6891 (Project ID:8390; PI: Hajian) reveal a prolate ellipsoidal nebula, as proposed by Guerrero et al. (2000), but neither the jet-like structures nor the other kinds of collimated outflows are apparent (Fig. 5, upper-left panels). Given that the [N II]/[O III] line ratio image unveils the faint LISs within the much larger scale structures of PNe (Corradi et al. 1996), we constructed the same image using the recent high-resolution HST images (Fig. 5, upper-right panel), where no jet-like structures are discerned. This provides additional confirmation of our previous conclusion, based on our low-dispersion spectra, that there are no jet-like structures in NGC 6891. The bottom panels in Fig. 5 display the radial profile of the [N II] and [O III] emission-line normalized fluxes (panels a and c) and the [N II]/[O III] line ratio (panels b and d) along the slits for the two PAs of 45° and 135° , respectively.

The ionic and chemical abundances of NGC 6891 are presented in Tables 11 and 13. NGC 6891 is a non-type I nebula due to its low He and N/O abundances. The chemical abundances for all nebular components, along both slit positions, are found to be the same, within the errors. Our chemical abundances of NGC 6891 agree with those derived from previous work (Wesson et al. 2005).

3.5 NGC 6572

NGC 6572, or PN G034.6+11.8, is a widely studied PN. Narrow-band images show an elliptical shell with the major axis oriented along $\text{PA} \sim 0^\circ$ and a seemingly toroidal structure (Miranda et al. 1999). The [N II]/[O III] image ratio highlights the presence of two pairs of knots at $\text{PA}=15^\circ$ and $\text{PA}=162^\circ$ (see Fig. 1 from Miranda et al. 1999). Both pairs are located at the tips of two much fainter collimated outflows, thus suggesting shock interactions. HST images of NGC 6572 do not confirm the presence of any knotty structure. Contrariwise, the HST $\text{H}\alpha/[\text{O III}]$ line ratio image reveals a filamentary structure around the collimated outflows indicating strong shock interactions (Guerrero et al. 2013),

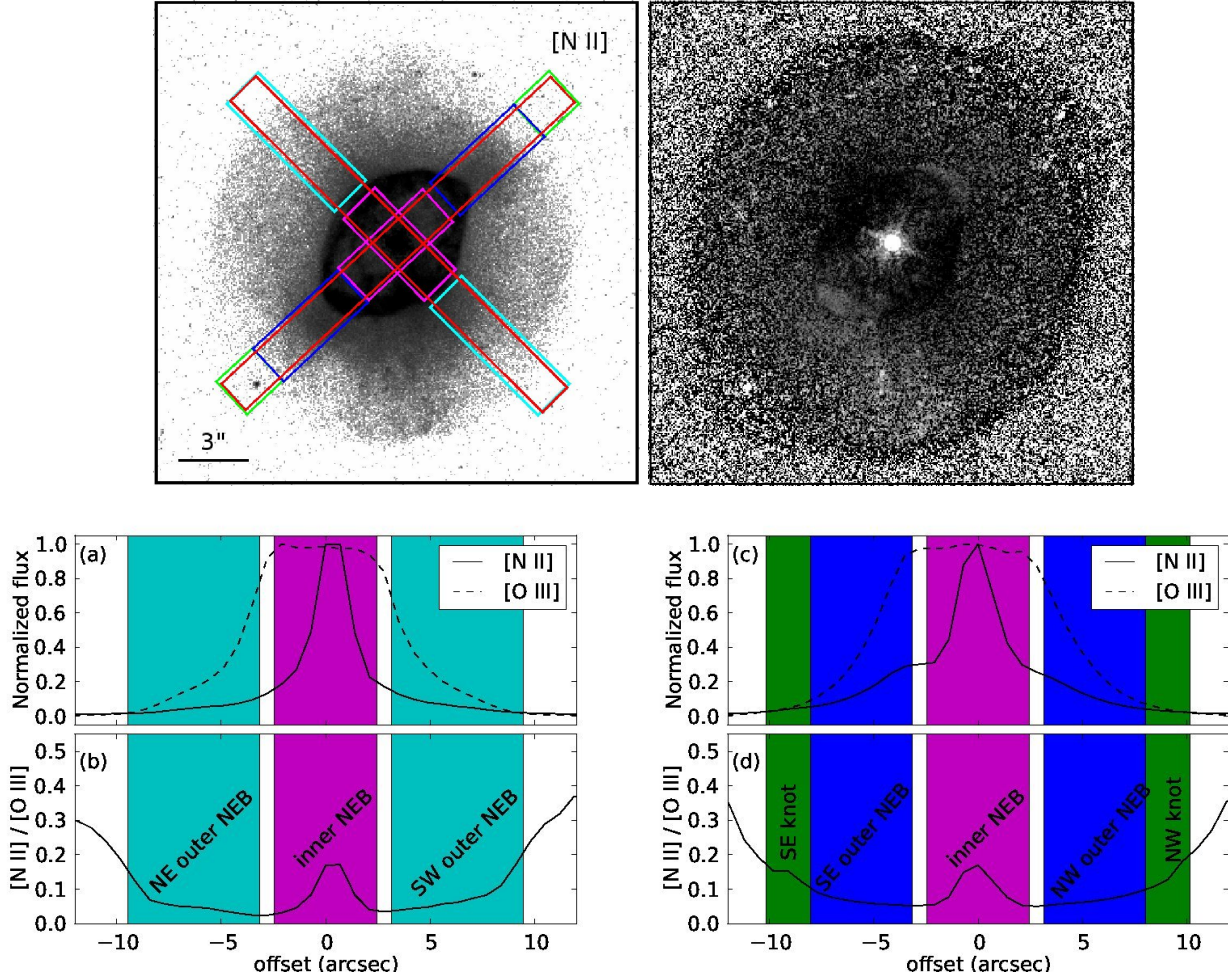


Figure 5. Upper panels: HST [N II] image (left-hand panel) and [N II]/[O III] line ratio image (right-hand panel) of NGC 6891. The size of the fields shown are $32 \times 32 \text{ arcsec}^2$ and $20 \times 20 \text{ arcsec}^2$, respectively. The nebular components under analysis are indicated. The extraction windows for these components are indicated by the corresponding boxes: the entire NW-SE and NE-SW nebular regions (entire NEB: 20.3 arcsec , in red); the NW and SE outer nebular regions (4.9 arcsec , in blue); NE and SW outer nebular regions (6.3 arcsec , in cyan); the SE and NW knots (2.1 arcsec , in green); and the inner nebular regions (inner NEB: 4.9 arcsec , in magenta). North is up, and East is to the left. Lower panels: The radial profile of the [N II] and [O III] emission lines fluxes, normalized to 1.0 and the [N II]/[O III] line ratio, along the slits: Panels (a) and (b) correspond to $\text{PA}=45^\circ$ whereas (c) and (d) to $\text{PA}=135^\circ$.

probably responsible for the narrow zones (shock fronts) and the enhancement of low-ionization lines.

The spectral type of NGC 6572 central star is still debatable. First, it was classified as a Of-WR type (Mendez et al. 1990), then as a WEL star (Tylenda et al. 1993; Parthasarathy et al. 1998), and more recently as a [WC]-PG 1159 star, by Marcolino et al. (2007). Narrow N III $\lambda\lambda 4634 - 41$ and C IV $\lambda 5808$ emission lines (with FWHM of 15 ± 2 and $20 \pm 3 \text{ \AA}$, respectively) are detected in our spectra, which is in agreement with the previous WEL-type or [WR] classification.

In order to study the physico-chemical properties of the nebula and the pairs of knots, two low-dispersion spectra were obtained along the $\text{PA}=15^\circ$ and 162° . The emission line fluxes as well as $c(\text{H}\beta)$, N_e and T_e are presented in the Tables 14 and 16. All the nebular structures used here are defined in Fig. 6. The [N II]/[O III] ratio profile of NGC 6572, along the two slits, are shown in Fig. 6 (panels c and d). $c(\text{H}\beta)$ varies slightly among the nebular component from

0.24 ± 0.05 to 0.29 ± 0.06 . These values are lower than those published by Liu et al. (2004; 0.48) and Frew et al. (2013; 0.41), but very close to the value derived by Kwitter et al. (2001; 0.32). Regarding the T_e , no variations were found between the inner nebula and the pairs of knots (see Table 14 and 16). Unlike T_e , N_e shows significant variations among the components. In particular, the knots are found to have lower density than the inner nebular regions, by a factor between 2 and 4. Moreover, the high densities derived from the Ar and Cl diagnostic line ratios imply a strong density stratification in its central region. $N_e[\text{S II}]$ is found to be lower than those previously published by Wang et al. (2004) and Kwitter et al. (2001), whilst $N_e[\text{Ar IV}]$ and $N_e[\text{Cl III}]$ are higher. The very high N_e of this nebula, close to the upper limit, indicate that any small change in the line ratio will result in substantial differences N_e values. This can explain the differences found in N_e among the aforementioned works and ours.

Tables 15 and 17 list the ionic and total abundances

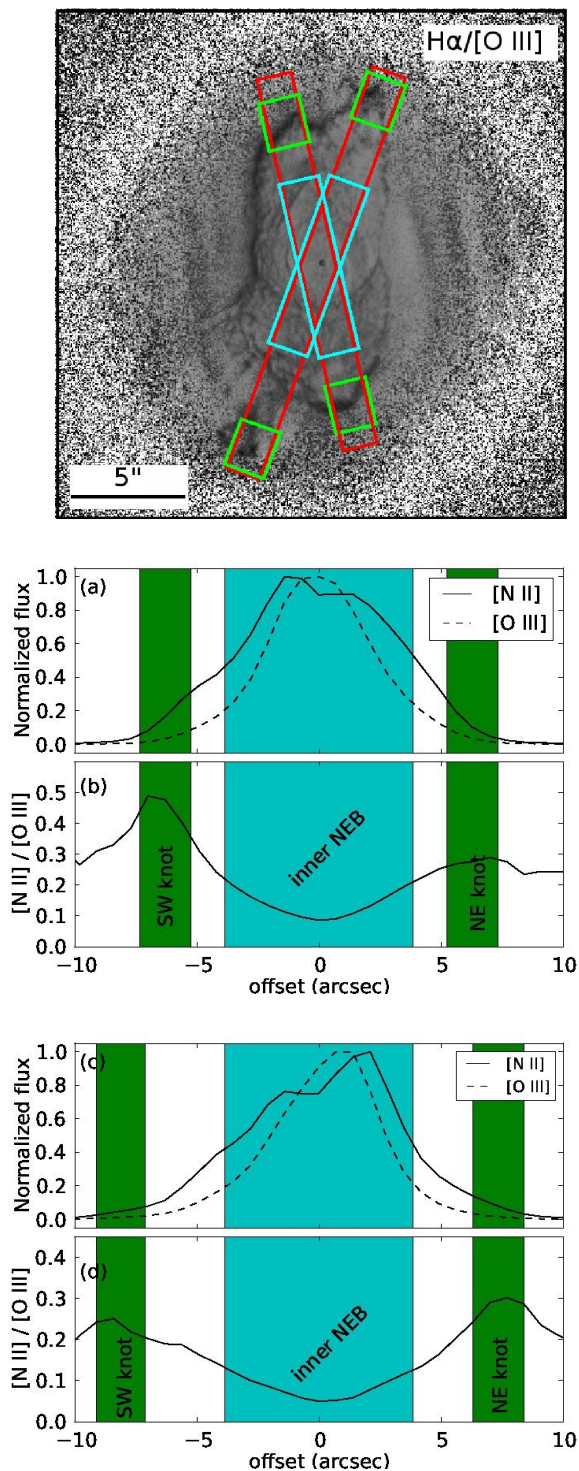


Figure 6. Upper panel: HST H α /[O III] image of NGC 6572. The size of the field shown is 22×22 arcsec². The nebular components under analysis are indicated in the image. The extraction windows for these components are indicated by the corresponding boxes: the entire nebular regions (entire NEB: 17.5 arcsec, in red); the inner nebular regions (inner NEB: 7.7 arcsec, in cyan); and the four, NE, NW, SE and SW knots (2.1 arcsec, in green). North is up, and East is to the left. Lower panels: The radial profile of the [N II] and [O III] emission-line fluxes, normalized to 1.0, and the [N II]/[O III] line ratio, along the slits. Panels (a) and (b) correspond to PA=11°, whereas (c) and (d) to PA=160°.

for all the nebular components of NGC 6572 and for both slit positions. We do not find any significant enrichment of N or S, with respect to the rest of the nebula that could be associated with the brighter [N II] and [S II] lines found in the knots. Chemical abundances for a given element are the same for all the components. Comparing our chemical abundances with those derived by Perinotto et al. (2004) and Henry et al. (2004), we turn out that He and N abundances agree with those from Perinotto et al. (2004), whilst O, Ne, and S abundances better agree with those from Henry et al. (2004). There is a substantial difference between these two studies. Moreover, the S knot (PA=160°) and the N knot (PA=15°) show enriched Ne abundance compared to the other two knots. Regarding our analysis, NGC 6572 is a non-type I PN, in contrast to the previous classification by Henry et al. (2004).

4 RESULTS: MORPHO-KINEMATIC PROPERTIES

Here we discuss the main morphological and kinematic characteristics of each nebula, and their different components, based on previously published works and echelle data taken from the SPM KCGPN. The wide range of expansion velocities of LISs, from a few tens to hundreds km s⁻¹ (Gonçalves et al. 2001), may suggest that shocks play a major role in the formation and excitation of these structures. Therefore, a parallel study of the morpho-kinematic and the physico-chemical properties (the emission line ratios, ionic and total chemical structure) is necessary to enlighten our knowledge of these structures. The de-projected expansion velocities of the nebular components, for each PN, are given in Table 1.

4.1 IC 4846

A morpho-kinematic analysis of IC 4846, performed by Miranda et al. (2001), reveals the presence of three pairs of elongated structures labelled as A1–A2 along PA=54°, and B1–B2 / C1–C2 along PA=11°. The authors claim that the components A1–A2 correspond to a high collimated precessing jet. The high-resolution HST H α image of IC 4846, presented here for the first time, provides further evidence that supports this hypothesis (see Fig. 2).

The projected expansion velocities of NE and SW jets range from 36 to 52 km s⁻¹, with an average value of 44 km s⁻¹ (Miranda et al. 2001). Considering that the inclination angle of the precession axis, with respect to the plane of sky, is 13–26°, the de-projected V_{exp} of the NE and SW jets are estimated to be between 100 and 190 km s⁻¹. The inner NEB of IC 4846 (or the C1–C2 features in Miranda et al. 2001) expands with a velocity of ~ 20 –25 km s⁻¹.

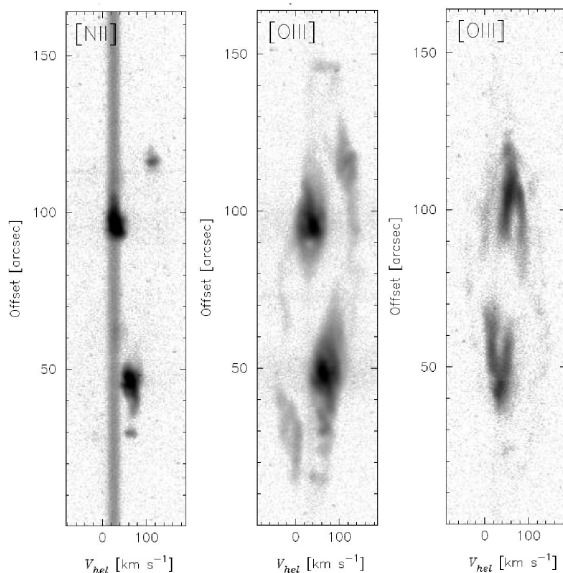
4.2 Wray 17-1

The kinematic study of this peculiar nebula has been performed by Corradi et al. (1999). The NW and SE filaments (labelled as A and B in Corradi et al. 1999) show a linear increase of expansion velocities up to ~ 30 km s⁻¹ in the [N II] emission line. Incidentally, the NW and SE knots at the outer parts of the nebula (labelled as A' and B' respectively in Corradi et al. 1999), show peculiar expansion

Table 1. De-projected expansion velocities of LISs and large-scales components. Errors are between 10% and 20% due to the uncertainties on the inclination angle.

PN name	PA ($^{\circ}$)	Jet/Jet-like or Filament (km s^{-1})	Jet/Jet-like or Filament (km s^{-1})	Knot (km s^{-1})	Knot (km s^{-1})	Inner NEB (km s^{-1})	Outer NEB (km s^{-1})
IC 4846	54	≥ 100 (NE)	≥ 100 (SW)	–	–	20–25	–
Wray 17-1	75	–	–	40–50 (W)	40–50 (E)	40	40 ^a
Wray 17-1	155	70–80 (NW)	60–70 (SE)	≥ 100 (NW)	≥ 40 (SE)	40	–
K 1-2	153	30–35	–	30–35 (NW)	30–35 (SE)	–	–
NGC 6891	45	–	–	–	–	10	28
NGC 6891	135	–	–	80 (NW)	80 (SE)	17	45
NGC 6572	15	–	–	46 (NE)	46 (SW)	18	–
NGC 6572	169	–	–	65 (NW)	55–65 (SE)	18	–

^a This expansion velocity refers to the E and W arcs.

**Figure 7.** Echelle spectra of Wray 17-1 drawn from KCGPN. Left panel: [N II], along PA=155 $^{\circ}$. Middle panel: [O III], along PA=155 $^{\circ}$. Right panel: [O III], along PA=75 $^{\circ}$.

velocities compared to the filaments. In particular, the NW and SE knots are found to be both red-shifted, with V_{exp} of $\sim 60 \text{ km s}^{-1}$ and $\sim 10 \text{ km s}^{-1}$, respectively, whilst the NW and SE filaments are blue and red-shifted, respectively. On the other hand, the E and W knots (respectively C and D, in Corradi et al. 1999) show expansion velocities of 15 km s^{-1} with the E knot being blue-shifted and the W knot red-shifted. The arc structures that surround these knots show similar expansion velocities.

High-dispersion [O III] PV diagrams along PA=60 $^{\circ}$ and 135 $^{\circ}$, were acquired from the SPM KCGPN to better constrain the morpho-kinematic structure of Wray 17-1 (Fig. 7). These PV diagrams clearly show the presence of an outer shell bright in the [O III] emission, but absent in the [N II] one. This structure expands with a velocity of 60 km s^{-1} , with the NW part red-shifted and the SE blue-shifted. The LISs seem to interact with the outer shell and indicate shock excitation.

If the central star of Wray 17-1 ejected stellar material along a geometrical cone, this could give a good explanation for the peculiar velocity field of the filaments and knots. In particular, the filaments could be the result of the interaction between the cone and the outer [O III] shell, whilst the NW knot, located exactly behind, and being well aligned with the filaments. Under this hypothesis, we can explain the blue-shifted NW filament and red-shifted NW knots. In the case of the SE filament and knot, this scenario implies that the two components are related. We calculate the inclination of this cone to 20–25 $^{\circ}$ with respect to the line of sight. This implies that the de-projected velocities of the filaments and the knots are at least 2.5–3 times higher. On other hand, the E and W knots are found to share the same expansion velocities of the surrounding nebula, with a de-projected velocity $\sim 40\text{--}50 \text{ km s}^{-1}$. The inner regions, NEB (NE, SW, NW and SE) appear to expand with a velocity of $\sim 40 \text{ km s}^{-1}$.

4.3 K 1-2

K 1-2 shows the presence of a collimated filament and several knots oriented along PA=–27 $^{\circ}$ (Corradi et al. 1999). These authors pointed out that all component appear to move with a velocity similar to that of the main nebula, 25 km s^{-1} , under the assumption that the NW filament (labelled A in Corradi et al. 1999) is located within the main spherically symmetric nebula. This assumption implies that the filaments and knots are oriented at a minimum inclination angle of 40 $^{\circ}$ with respect to the line of sight. Given that the inclination angle of the spectroscopic binary has been determined 50 $^{\circ}$ (Exter et al. 2003), the de-projected expansion velocity of the knots and jet-like structure would be $\geq 30\text{--}35 \text{ km s}^{-1}$.

4.4 NGC 6891

Guerrero et al. (2000) studied the kinematic properties of this nebula and reached the conclusion that a highly-collimated outflow (jet) is present along PA=135 $^{\circ}$. The maximum de-projected velocity is 80 km s^{-1} , at the outer edges (A–A' component or the pair of knots), considering an inclination angle with respect to the plane of sky of 10 $^{\circ}$. Re-

garding the inner and outer NEB, the authors adopted an ellipsoidal shell model with a homologous expansion law to reproduce the observed data. They concluded that the inner NEB expands with a velocity of 10 km s^{-1} along the minor (PA=45°) and 17 km s^{-1} along the major axis (PA=135°), while the outer NEB expands faster with $V_{\text{exp}}=28\pm 5 \text{ km s}^{-1}$ along the minor (PA 70°) and $45\pm 5 \text{ km s}^{-1}$ along the major axis (PA~160°).

4.5 NGC 6572

Following Miranda et al. (1999), NGC 6572 shows the presence of two pairs of low-ionization knots oriented along PA=15° and PA=-18°. Moreover, two, much fainter, ellipsoidal structures can also be discerned in these directions. Fig. 6 shows, in fact, that the two pairs of knots are not really low-ionization nebular condensations, but resemble those of knots due to the low angular resolution of the ground-based images. We think that these knots actually result from the interaction between the outflows and the outer shell (AGB envelope), consistent with theoretical shock models (Dopita 1997; Raga et al. 2008).

The projected expansion velocity is 39 km s^{-1} for the NW and the SE knots, and 8 km s^{-1} for the NE and SW knots. It is worth mentioning here that the SE knot shows a peculiar decreasing velocity, from 38 to 33 km s^{-1} (Miranda et al. 1999). The NGC 6572 inner NEB shows a projected velocity of 14 km s^{-1} . Moreover, two clearly separated maxima are discerned in the PV diagrams, indicating the presence of a $\sim 14 \text{ km s}^{-1}$ toroidal structure at the centre of the nebula. This toroidal component has an inclination angle of 38° with respect to the plane of sky (Hora et al. 1990; Miranda et al. 1999). In accordance with this inclination angle, the de-projected expansion velocities are calculated to 18 km s^{-1} for the torus and the inner NEB, $\sim 65 \text{ km s}^{-1}$ for the NW knot, and $\sim 55\text{--}65 \text{ km s}^{-1}$ for the SE knot. The ellipsoidal structure along PA=15° is less tilted, by $\sim 10^\circ$, and we obtain a de-projected velocity of $\sim 46 \text{ km s}^{-1}$ for both the NE and the SW knots.

5 DISCUSSION

5.1 Electron temperatures

T_e was estimated for several individual regions e.g., knots, filaments, jets and jet-structures, inner and outer nebular regions and arcs, as well as the entire nebulae. We mainly used the [O III], [N II] and [S II] diagnostic lines. T_e is found to range between 9700 K and 14700 K, which is typical of photo-ionized nebula, with an average of $T_e[\text{O II}]$ of 11500 K and $T_e[\text{N II}]=11340$ K. Moreover, among the various nebular components, no significant variation in T_e is found, which agrees with previous studies (e.g. Gonçalves et al. 2009; and references therein).

5.2 Electron densities

Regarding the electron densities, previous studies on the main nebular components (rims and shells) versus LISs have shown that the latter have systematically lower densities than the former, by a factor between 1 and 10 (see Gonçalves

et al. 2009; and references therein). This result comes into conflict with the theoretical predictions, on which the LISs are denser than the surrounding medium.

The most likely explanation for this discrepancy between models and observations may be that the models are referred to the total density of gas (dust, atomic and molecular as well) while N_e corresponds only to the ionized fraction of the gas (Gonçalves et al. 2009). In this work, we confirm that LISs have the same or even lower densities than their surrounding medium. Indeed, in a paper in prep. we report our first successful detection of the molecular hydrogen emission, at $2.12 \mu\text{m}$, associated to the LISs of two PNe (K 4-47 and NGC 7662). Although, this detection was tried before by the group, the fact that LISs have in general smaller scales than the main bodies did not help. It seems that only 8-m class telescopes can successfully detect the H_2 associated with LIS in Galactic PNe. See Machado et al. (2015) for a similar work, though not associated with LISs directly, but with the molecular torus of NGC 2346. Moreover, it turns out that the molecular torus of this PN is composed of knots and filaments. On the other hand, in the Helix nebula (Meaburn et al. 1992; Odell & Handron 1996; Huggins et al. 2002), which posses the best-known LISs of PNe, the association between LISs and the molecular gas is known for years.

Images of PNe in molecular hydrogen (H_2) and optical emission lines (e.g. [N II], [S II] and [O I]) display similar morphologies (Guerrero et al. 2000; Bohigas 2001). In accordance with the theoretical work by Aleman & Gruenwald (2011), the peak intensities of these optical lines and the H_2 $v=1\text{--}0$ co-rotational lines occurs in a narrow transition zone between the ionized and the neutral (photo-dissociation) regions. It is known that molecular hydrogen in PNe can be excited either by shocks or by the absorption of UV-photons (fluorescence) emitted by the central star. Therefore, the detection of strong [N II] and [O I] emission lines in LISs may be the result of shock excitation, due to the moderate expansion velocities (see § 4).

Shock models can successfully reproduce the strong low-ionization lines from LISs (K 4-47; Gonçalves et al. 2004; Raga et al. 2008). In particular, Raga et al. (2008) reached the conclusion that the lower the photo-ionization rate, the higher the N_e diagnostic line ratios, which then resemble the typical values of shock-excited regions. Besides the expansion velocities of LISs, the evolutionary age and photo-ionization rate of the central source are also key parameters for probing the excitation and formation mechanisms of LISs, thus unveiling their true nature.

5.3 Ionic and total abundances

The chemical abundances were calculated for the several nebular components used here for the analysis of the 5 PNe. Comparison with those abundances derived in previous studies shows a reasonable agreement with previous results, not only for the entire nebulae but also for each component individually.

For a given PN, and element, all the components exhibit the same chemical abundances, within the uncertainties. This implies that the strong low-ionization lines, such as [N II], [S II] or [O I] of LISs, may not be the result of an overabundance of these elements in the nebula. Fig. 8

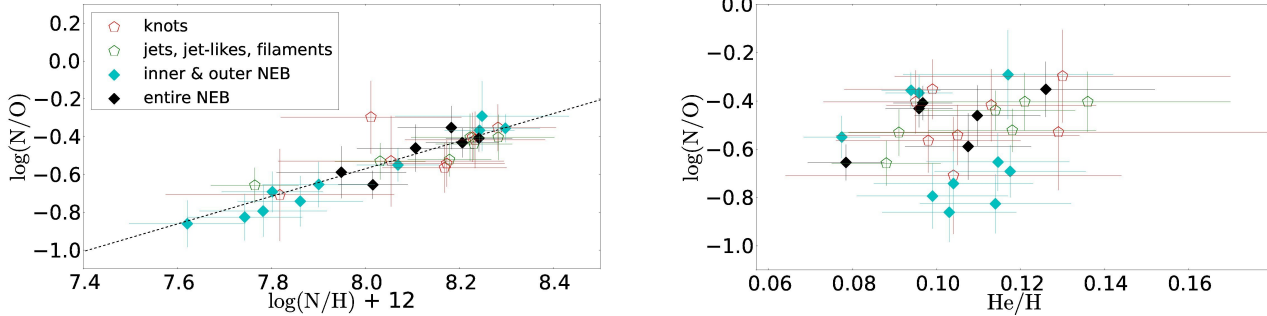


Figure 8. Abundance patterns: $\log(N/O)$ vs. He/H (left-hand panel) and $\log(N/O)$ vs. $\log(N/H)+12$ (right-hand panel). Red pentagons correspond to LISs, green pentagons to jets, filaments and jet-like structures. Nebular regions (inner and outer NEBs) are cyan filled diamonds whilst the entire NEBs are black filled diamonds. The dashed line represents the best linear fit to our data (see text).

displays $\log(N/O)$ vs. $\log(N/H)+12$ (left-hand panel) and $\log(N/O)$ vs. He/H (right-hand panel) for all the PNe in our sample and their components. A linear relation between $\log(N/O)$ and $\log(N/H)+12$ is found, which is consistent with the general picture for PNe (Perinotto et al. 2004). The best linear fit to our data yields the relation, $\log(N/O)=0.74*(\log(N/H)+12)-6.5$, with R^2 (the goodness-of-fit) equals to 0.88, and it is in very good agreement with the relation derived from a sample of PNe with WR and WEL-type central stars (García-Rojas et al. 2013). Only E knot in Wray 17-1 appears as an outlier (easily identifiable in the figure), so not considered in the fitting process. The $\log(N/O)$ vs. He/H plot does not show any correlation between the LISs and the other nebular components, whereas both show $He/H < 0.14$ and $\log(N/O) < -0.3$. These figures, following Kingsburgh & Barlow (1994) criteria, implies that all the PNe in our sample are non Type-I nebulae.

In Fig. 9 we plot $\log(X/O)$ vs. $\log(X/H)+12$ for $X=Ne, S$ and Ar , and clear linear trends are found. We have to mention that the apparent distinct regions in these diagrams do not really reflect chemical abundance differences between LISs and other nebular components (NEBs), but potential differences between the PNe in our sample and their central stars. For instance the LISs with $Ne/O > 0.55$ and $\log(Ne/H)+12 > 8.1$ (as well as $Ar/O > -2.5$ and $\log(Ar)+12 > 6.1$) correspond to the LISs in K 1-2 and Wray 17-1, for which we were able to estimate their Ne and Ar abundances, whereas the NEBs are those from IC 4846, NGC 6572 and NGC 6891. Thus, K 1-2 and Wray 17-1 are likely richer, in Ne and Ar, than the rest of the PNe in our sample. Surprisingly, LISs in the former PNe are highly-ionized, with He being mainly doubly ionized (see Tables 5, 7 and 9). As for S, all the components (LISs and NEBs) are well mixed and cover the same range of values. Trends we found in Figure 9 are those usually seen in PNe between the α -element to oxygen ratios.

In conclusion, the similarities in the chemical abundances among the components in each PN strongly suggest that the intense low-ionization emission lines are the result of their excitation mechanisms rather than the chemical overabundance of any element in the LISs.

Moreover, though a deep discussion about the abundance discrepancy factor (*adf*) is out of the scope of the present paper, it is relevant to note that *adfs*, close binaries as PN central stars (so, post CE stars) and the presence of

LIS could somehow be related. As briefly discussed in the Introduction, the formation LIS, and particularly that of jets older than the main shells, is expected in the case of post common-envelope PN central stars (Gonçalves et al. 2001; Miszalski et al. 2011). Very recently, it was shown that the PNe having the highest *adfs* (10 to 300) all have post CE central stars (Corradi et al. 2015). In addition of confirming the mixing of the bi-chemistry in these PNe (hot normal component plus hydrogen-deficient cold inclusions; Liu et al. 2004), Corradi et al. (2015) point out the present difficult in depicting an evolutionary scenario consistent with all the observed properties of the highest *adf* PNe. Some of the scenarios these authors discuss could indeed be related with the presence of LISs via, for instance, the photo-ionization of the neutral material that was in the orbital plane during the CE phase.

5.4 Excitation mechanism

Besides the emission line ratios, kinematic information –in fact expansion velocities– is essential to fathom the formation and excitation mechanisms of LISs in PNe. The diagnostic diagrams, based on the shock models from Raga et al. (2008), are used here in order to perform a more comprehensive study on the LISs and the other nebular components by combining their emission lines and expansion velocities.

In particular, Raga et al. (2008) modelled the evolution of a high-speed ($100\text{--}150 \text{ km s}^{-1}$) and high-density (10^3 cm^{-3}) knot moving away from a photo-ionizing source through a low-density medium, for a range of initial conditions. The simulated knot is a spherical cloudlet with temperature of 10000 K, and size of 10^6 cm . The surrounding medium was assumed to be uniformly filled with a low-density gas of 10^2 cm^{-3} and the same temperature (10000 K) of the knot. A black-body approximation was assumed for the central photo-ionizing source, with a $L=5000 L_{\odot}$ and two T_{eff} of 50000 K and 70000 K, which correspond to an ionizing photon rate of $S_{\nu}=3.41 \times 10^{47} \text{ s}^{-1}$ and $4.66 \times 10^{47} \text{ s}^{-1}$, respectively. Moreover, the effect of the distance between the knot and the central source was also studied for three specific distances of 3, 1, $0.3 \times 10^{18} \text{ cm}$.

The emission line ratios of the knots, for two different epochs of the simulations (200 yr in red and 400 yr, in green), are presented in Fig. 10, superposed to the ob-

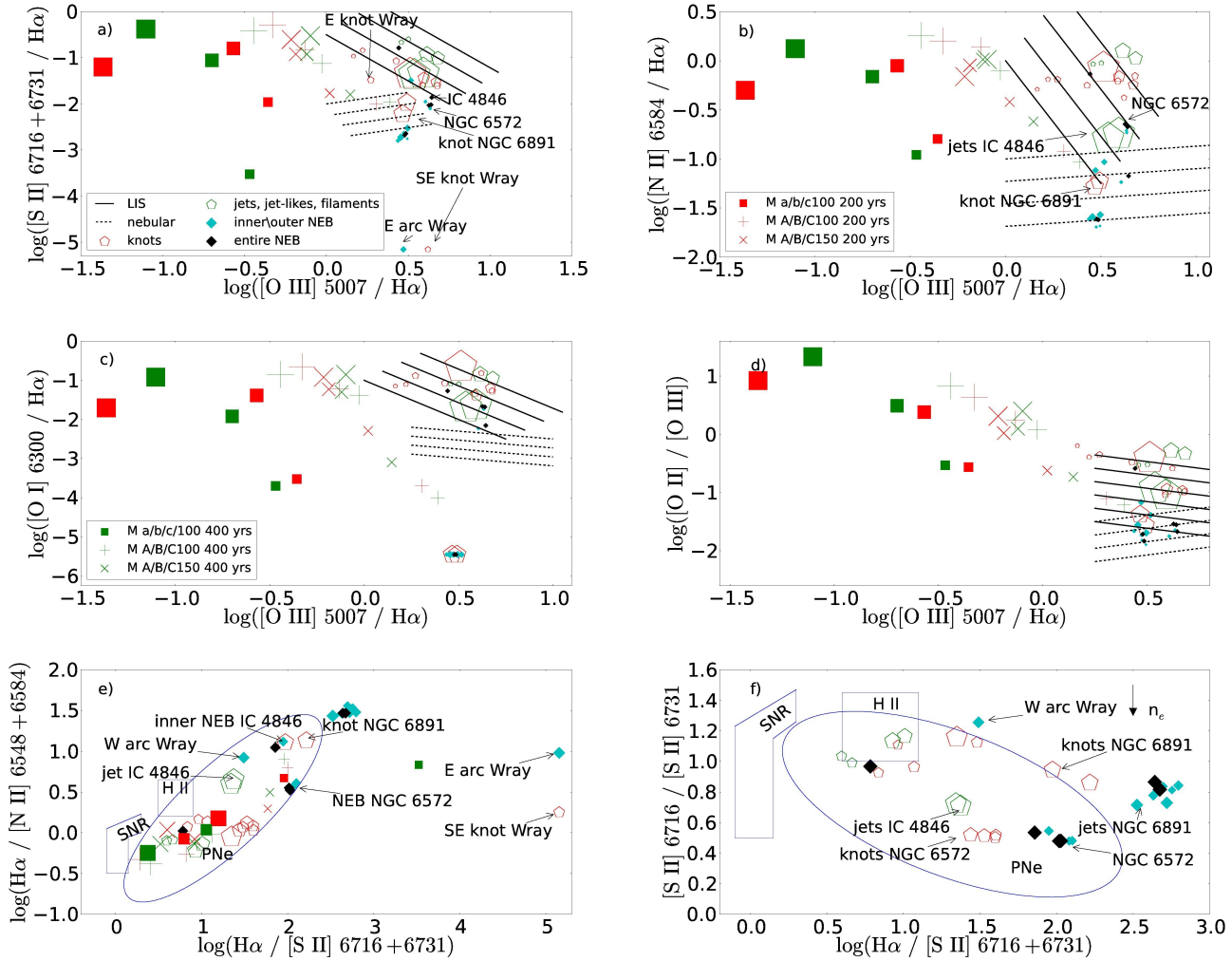


Figure 10. Diagnostic diagrams distinguishing the shock-excited and the photo-ionized regions. Panels a, b, c, and d are the diagnostic diagrams from Raga et al. (2008), on which we superimpose the results for our sample of PNe. The regions with diagonal solid lines represents the loci of fast LISs, whereas the regions with dashed lines represent the location of photo-ionized structures (e.g. inner and outer NEBs that are in fact shells and rims). Panels e and f display the diagnostic diagrams by Sabbadin et al. (1977), with the density ellipses introduced by Riesgo & López (2006).

served emission line ratios from this work. Unfortunately, these models do not provide any predictions for the properties of the other nebular components like shells, rims and haloes. The symbols in Fig. 10 correspond to different expansion velocities, T_{eff} , and distances to the central source. –boxes: $V_{\text{exp}}=100$ km s $^{-1}$ and $T_{\text{eff}}=50000$ K (models a/b/c100); crosses: $V_{\text{exp}}=100$ km s $^{-1}$ and $T_{\text{eff}}=70000$ K (models A/B/C100); and x symbols: $V_{\text{exp}}=150$ km s $^{-1}$ and $T_{\text{eff}}=70000$ K (model A/B/C150). Letters from “a” to “c” (and “A” to “C”) indicate the different distances from the central source and thus the different photo-ionization rates (small symbol \equiv small distance \equiv closer to the central source). The solid and dash-dotted lines enclose the regime of fast LISs (e.g. knots, jets) and rims and shells (or, more general, photo-ionized regions) taken from Raga et al. (2008). The open pentagons correspond to the LISs (knots: red and jets/jet-likes/filaments: green), the filled cyan diamonds correspond to the inner and outer NEB regions, and the filled black diamonds to the entire NEB. Moreover, the

larger the points’ size the higher the de-projected expansion velocity (see Table 1). The velocities are normalized to the average expansion velocity of PNe, 31 km s $^{-1}$ (Pereyra et al. 2013). For the entire NEB (black symbols), we considered an expansion velocity equal to the value just quoted, so emphasizing the different expansions among the nebular components in the diagnostic diagrams. No trend is found between the emission line ratios and V_{exp} of the LISs and the nebular regions. This suggests that any attempt to disentangle the photo-ionized and shock-excited regions, or even investigate their excitation mechanisms, requires the evolutionary age and photo-ionization rates of the central star, apart from the expansion velocities themselves.

All LISs in this work are found to be located in the regime of fast LISs, except from the pair of knots in NGC 6891. The latter knots are displaced from the region of fast LISs, in each diagram, despite their high expansion velocities. Moreover, the NE and SW outer NEBs in NGC 6891 (the jet components in Guerrero et al. 2000) also lie in the

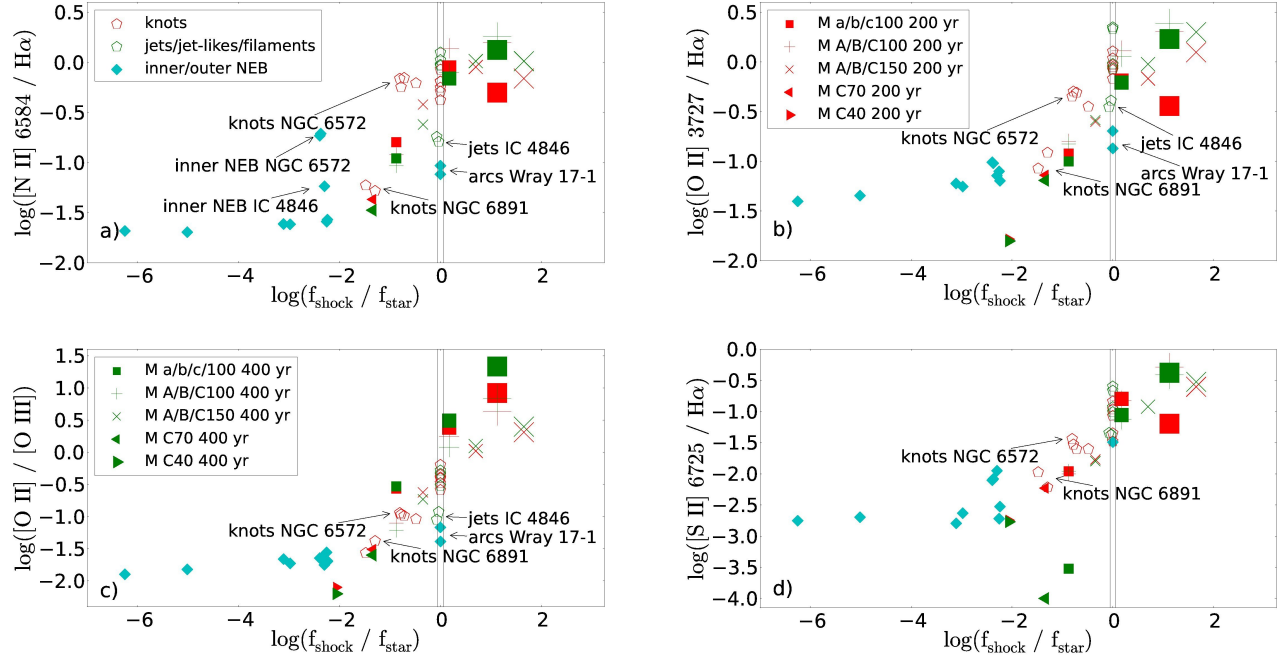


Figure 11. Plots of $[N II]/H\alpha$ (panel a), $[O II]/H\alpha$ (panel b), $[O II]/[O III]$ (panel c) and $[S II]/H\alpha$ (panel d) vs. $\log(f_{shocks}/f_*)$. The vertical strips represent $\log(f_{shocks}/f_*) = 0$. K 1-2 and Wray 17-1 structures were arbitrarily placed into the strips, since there are no distance measurements for these PNe.

regime of photo-ionized regions and close to the inner NEBs of the nebula (NE and SW outer NEBs). This is a further indication that there is no difference among the regions analyzed in NGC 6891. We already pointed out that there are no jets in NGC 6891 (see §3.4). Knots, on the other hand, show low-ionization lines slightly enhanced. We believe that this may be associated with the low contribution of the photo-ionization in these knots (higher distance from the central star), resulting in more efficient shock excitation.

Adopting a distance of 2.5 kpc for NGC 6891 (Phillips 2005) and an angular distance from the central star of 9.1 arcsec, the linear distance is $\sim 3.4 \times 10^{17}$ cm. Given that the T_{eff} and L of the central star are 50000 K (Mendez et al. 1988) and $10000 L_{\odot}$ (Mendez et al. 1992; re-scaled to the distance used here), respectively, the ionizing photon flux (f_*) reaching the knots is $f_* = 5.46 \times 10^{11} \text{ cm}^{-2} \text{ s}^{-1}$. NGC 6891's knots lie closer to the Raga's C100 model ($V_{exp} = 100 \text{ km s}^{-1}$, $D = 3 \times 10^{17} \text{ cm}$ and $f_* = 3.73 \times 10^{11} \text{ cm}^{-2} \text{ s}^{-1}$) than to the c100 model ($V_{exp} = 100 \text{ km s}^{-1}$, $D = 3 \times 10^{17} \text{ cm}$ and $f_* = 2.73 \times 10^{11} \text{ cm}^{-2} \text{ s}^{-1}$). The main difference between these two models is the ionizing photon flux, which depends on the T_{eff} . Models ‘‘C’’ are those with the smallest distance from the central stars and therefore have higher ionization rates. Hence, NGC 6891 appears to be a nebula with a higher ionization rate (so, mainly photo-ionized) whilst the contribution of shocks must be very low. Nevertheless, the high expansion velocities of the pair of

knots ($\sim 80 \text{ km s}^{-1}$), results in the enhancement of the low-ionization lines.

As for NGC 6572, the inner NEBs are in a transition zone between the rims/shells and fast LISs regimes, whilst the two pairs of knots are well placed on the regime of the fast LISs. The de-projected expansion velocities of the two pair of knots are at least 2.5–3 times higher than the expansion velocities of the inner NEBs, then suggesting higher contribution from shocks. The angular distances of the knots from the central star are 6.67 arcsec (NE and SW), 7.5 arcsec (NW) and 8.4 arcsec (SE). Considering a distance of 1.4 kpc (Mellema 2004), we obtain linear distances from the central star of 1.35 , 1.5 and 1.71×10^{17} cm. These distances give ionizing photon fluxes between 2.3 and $3.4 \times 10^{10} \text{ cm}^{-2} \text{ s}^{-1}$, considering $T_{eff} = 60000 \text{ K}$ and $L = 2250 L_{\odot}$ (Shaw & Kaler 1989; re-scaled to distance adopted in this work). This ionizing photon fluxes imply a low contribution in the excitation of the knots due to the absorption of UV photos. Therefore, the enhancement of the low-ionization lines in these structures should be a result of the shocks. The higher ionizing photon flux of the inner NEBs, due to their smaller distance to the central star, in conjunction with their much lower expansion velocities, explain their position on the diagnostic diagrams in the regime of photo-ionized regions.

Unlike the knots of NGC 6572, the jets of IC 4846 are located in the transition zone, despite their high expansion velocities ($> 100 \text{ km s}^{-1}$). For $T_{eff} = 50000 \text{ K}$ and $L = 2067 L_{\odot}$ (Shaw & Kaler 1989; rescaled to the distance used here), the ionizing photon rate is $1.36 \times 10^{47} \text{ s}^{-1}$, and for an angular distance from the central of 3.5 arcsec and $D = 5.72 \text{ kpc}$ (Phillips 2004), the linear distance is then $3 \times 10^{17} \text{ cm}$. This implies an $f_* = 1.20 \times 10^{11} \text{ cm}^{-2} \text{ s}^{-1}$, which is approximately three times lower than that of C100 model. Despite

¹ The ionizing photon flux, f_* , is calculated by means the equation $f_* = S_* 4\pi d^2$, where S_* is the photon rate and d is the distance of the cloudlet from the central star.

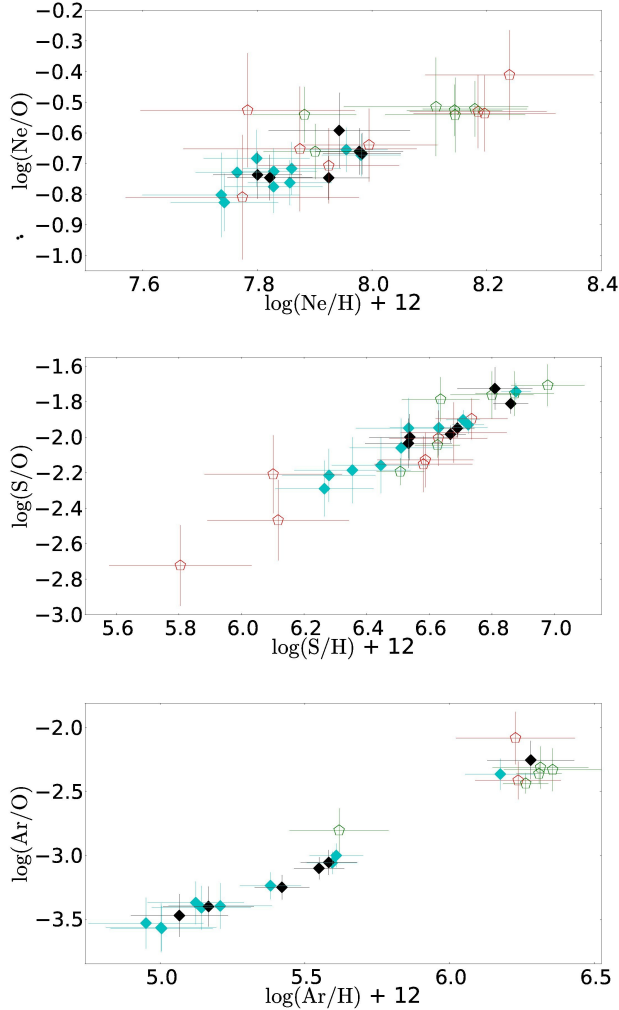


Figure 9. Abundance patterns: $\log(\text{Ne}/\text{O})$ vs. $\log(\text{Ne}/\text{H})+12$ (upper panel); $\log(\text{S}/\text{O})$ vs. $\log(\text{S}/\text{H})+12$ (middle panel) and $\log(\text{Ar}/\text{O})$ vs. $\log(\text{Ar}/\text{H})+12$ (lower panel). Symbols are the same as in Fig. 8. A trend of increasing Ne/O, S/O and Ar/O with increasing Ne, S and Ar, respectively, is found.

this low value, IC 4846 exhibits stronger [N II], [S II] and [O I] emission lines than in model C100, which means that shock interactions are responsible for this enhancement.

All LISs of Wray 17-1 are well placed in the regime of fast LISs, with intense low-ionization lines. Unfortunately, there is no distance measurement for this object. Nevertheless, assuming a linear distance of 3×10^{17} cm between the knots and the central star (the smallest distance among the shock models), and an angular distance of 43 arcsec from the central source, a $D = 0.46$ kpc is obtained, which seems unrealistic. This may suggest that the knots are at a larger distance from the central star, e.g. 3×10^{18} cm (or $D \sim 5$ kpc). We believe that the strong low-ionization lines found in this nebula are resulting from shocks, whilst the contribution of the stellar UV photons may be very low. The observed spectra from the inner NEBs are in agreement with this argument.

Regarding the $\text{H}\alpha/[\text{N II}]$ vs. $\text{H}\alpha/[\text{S II}]$ and $[\text{S II}]/\lambda\lambda 6716/6731$ vs. $\text{H}\alpha/[\text{S II}]$ diagnostic diagrams, introduced

by Sabbadin et al. (1977), it is clear that all shock-excited features are located at the bottom-left region whilst the photo-ionized features at the upper-right region (lower panels in Fig. 10). The zone between $0.2 < \log(\text{H}\alpha/[\text{N II}]) < 0.8$ defines the transition zone where both excitation mechanisms are efficient. In general, hot and dim central stars are able to reproduce emission lines ratios that resemble those of shock-excited nebulae without necessarily being shocked-excited (Raga et al. 2008). This could explain the presence of some elliptical and round PNe in the region with $\log(\text{H}\alpha/[\text{N II}]) < 0$ and $\log(\text{H}\alpha/[\text{S II}]) < 0.4$ (Sabbadin et. 1977; Riesgo & Lopez 2006).

In accordance to the previous analysis, besides the emission line ratios, kinematic information is required in order to probe the excitation mechanisms of the LISs in PNe. Hence, a more general approach, which would take into account the contribution of shock- and photo-ionization is actually required here. We quantitatively investigate this by defining the dimensionless parameter $\log(f_{\text{shocks}}/f_{\star})$, where f_{shocks} is the ionizing photon flux in units of $\text{cm}^{-2} \text{s}^{-1}$ for a shock with V_s , and f_{\star} is the stellar ionizing photon flux at a given distance. f_{shocks} is as follows: we calculate the total energy flux emitted due to the shock, by using the formula $F_{\text{shocks}} = 2.28 \times 10^{-3} (V_s/100 \text{ km s}^{-1})^3 \times (n_e/\text{cm}^{-3})$ in units of $\text{erg cm}^{-2} \text{s}^{-1}$ from Dopita & Sutherland (1996). Then, we convert this energy flux (F_{shocks}) to photon flux (f_{shocks}), by dividing by the average energy of a photon (L/S_{\star}) emitted from the central star. This ratio should give us of the contribution of each mechanism to the excitation of the gas.

In Fig. 11 we present the new diagnostic diagrams $[\text{N II}]/\text{H}\alpha$, $[\text{S II}]/\text{H}\alpha$, $[\text{O II}]/\text{H}\alpha$ and $[\text{O II}]/[\text{O III}]$ vs. $\log(f_{\text{shocks}}/f_{\star})$ that allows us to distinguish nebular components with different excitation mechanisms. It is noticeable that there are two distinct regimes in these diagrams: i) the upper-right corner with the shock-excited structures and ii) the lower-left corner with the photo-ionized structures. A transition zone, where both excitation mechanisms are important, can also be considered. All the nebular regions (NEB) lie in the lower-left region, with $\log(f_{\text{shocks}}/f_{\star}) < -2$, whilst the knots and jets lie in the upper-right part of the diagrams, with $\log(f_{\text{shocks}}/f_{\star}) > -1$. Only the pair of knots in NGC 6891 show $\log(f_{\text{shocks}}/f_{\star}) < -1$, consistently with our previous conclusion that they must be mainly photo-ionized with a low contribution from shocks. The models a/b100, A/B100 and A/B150 also lie in the shock-excited regime (upper-right corner), whilst the models c100, C100 and C150 are found in the transition zone. The latter models have the higher ionizing photon flux among all the models, which means that the excitation due to the absorption of stellar UV photons is more efficient. Any decrease of V_{exp} , for instance from C100 to C70 or C40, will result in further decrease of $\log(f_{\text{shocks}}/f_{\star})$ and will eventually place these models closer to the regime of photo-ionized regions.

The points representing K 1-2 and Wray 17-1 have been arbitrarily added to the diagram, at $\log(f_{\text{shocks}}/f_{\star}) = 0$, since there are no distance measurements for these objects and the f_{\star} cannot be calculated. Based on their emission line ratios, one can assume that the jets and knots of these two objects have, indeed, $\log(f_{\text{shocks}}/f_{\star})$ close to 0. Assuming $\log(f_{\text{shocks}}/f_{\star}) = 0$ for the knots and jets, $\log(f_{\text{shocks}}/f_{\star}) = -1$ for the arcs, and $L = 5000 L_{\odot}$, we obtain a rough estimation of their distances. Wray 17-1 should be located between 3

and 7 kpc, where for K 1-2, we obtain a very high distance, >20 kpc. This suggests that the luminosity of the central star in K 1-2 is lower than $5000 L_{\odot}$ and/or the expansion velocities of the knots are higher than 35 km s^{-1} . For instance, a $L=2000 L_{\odot}$ and $V_{exp}=70 \text{ km s}^{-1}$ gives us a more reasonable distance of $\sim 5 \text{ kpc}$.

5.5 Central Star

Despite the various attempts to explain the formation of collimated (those that appear in pairs) LISs, their origin still remains debatable (see in Gonçalves et al. 2001). The most prominent mechanism is the interaction of a close binary system due to the mass-transfer exchange. The formation of an circumstellar/circumbinary disk via binary interaction provide those conditions to form bipolar outflows and/or collimated jets (Blackman et al. 2001, Nordhaus & Blackman 2006). Some models suggest that the formation of jets occurs after the common envelope (CE) phase of a close binary star (Soker & Livio 1994). Pairs of jets with kinematical ages much younger than the main nebular structures have indeed been found in some post-CE PNe, like NGC 6778 and NGC 6337 (Tocknell et al. 2014). Although, the majority of the post-CE PNe are found to exhibit jets that predate the main nebular structures, suggesting that the polar ejection occurs before the CE phase (see Tocknell et al. 2014; Jones et al. 2014). The discovery of several new close binary stars in PNe has provided strong evidence of a link between the close binary post-common envelope PNe and LISs (Miszalski et al. 2009b).

Moreover, a possible link between the spectral type of the PN nucleus and LISs has also been pointed out by Miszalski et al. (2009a). According to these authors, more than half of PNe that are known to possess LISs ($\sim 65\%$) have an emission line type central star (e.g. Of, [WR] or PG1159). Incidentally, all the PNe studied in this work have an emission-line star, except K 1-2. In particular, two of them have a WEL type nucleus (IC 4846, NGC 6891), one has a [WC]–PG1159 (NGC 6572), and one a PG–1159 nucleus (Wray 17-1). The central star of K 1-2 has been classified as a K2 V but it is a known post-CE close binary system (Exter et al. 2003; De Marco 2009).

6 CONCLUSIONS

The properties like N_e , T_e , ionic and total chemical abundances were calculated for various nebular components, like nebular regions (inner and outer NEBs) and LISs (jets, jet-like, filaments and knots), as well as for the entire nebulae of a small sample of PNe (IC 4846, Wray 17-1, K 1-2, NGC 6891 and NGC 6572). We confirmed that LISs are less dense (in terms of N_e) than the surrounding medium, whereas their T_e are the same as that of the other components of a given PNe.

There is no chemical abundance enrichment in LISs that could be attributed to the strong low-ionization lines. For a given PN, all the nebular components have the same chemical abundances within the errors, reflecting on the chemical composition of the entire nebula as well as the evolution of the central star.

A comparison of between the emission lines of the nebular components and those predicted by the the shock models reveals that LISs are predominantly shock-excited regions. This shock-excitation of LISs results in the enhancement of the low-ionization lines, whereas the other nebular components are mainly photo-ionized, so less prominent in the low-ionization emission lines.

In order to probe the contribution of shocks and UV photons in the excitation of the LISs, we defined the parameter $\log(f_{shocks}/f_{\star})$, where f_{shocks} and f_{\star} are the ionizing photon fluxes due to the shock interactions and the central star continuum, respectively. We then proposed new diagnostic diagram that involves the emission-line ratios $[N \text{ II}]/H\alpha$, $[O \text{ II}]/H\alpha$, $[S \text{ II}]/H\alpha$ and $[O \text{ II}]/[O \text{ III}]$ versus the new excitation parameter, $\log(f_{shocks}/f_{\star})$. A robust relation differentiating the regimes of shock-excited ($\log(f_{shocks}/f_{\star}) > -1$) from that of the photo-ionized components ($\log(f_{shocks}/f_{\star}) < -2$), in addition to a transition zone ($-2 < \log(f_{shocks}/f_{\star}) < -1$), where both mechanisms are equally important, is found. Most of the LISs analyzed in this work were found to be well located in the regime of shock-excited structures, apart from the pairs of jets and knots in NGC 6891. The former was found to be photo-ionized as much as its surrounding nebula, while the latter is placed in the transition zone, which indicates a contribution from shocks. All the inner and outer NEBs are well placed in the region of the photo-ionized components.

ACKNOWLEDGMENTS

We thank, enormously, R. Corradi and H. E. Schwarz (in memoriam) who provide us the Danish telescope data we use in the present paper. We also would like to thank the anonymous referee for his/her detailed report on the manuscript, which indeed helped us to significantly improve the paper. The work of SA is supported by CAPES post-doctoral fellowship ‘Young Talents Attraction’ - Science Without Borders, A035/2013. This work was also partially supported by FAPERJ’s grant E-26/111.817/2012 and CAPES’s grant A035/2013. The analysis here presented is based on observations obtained at the 2.5-m INT (IDS), operated by the Isaac Newton Group on the island of La Palma in the Spanish Observatorio del Roque de los Muchachos of the Instituto de Astrofísica de Canarias. Our work is also based on the 1.54-m Danish telescope (DFOSC) data, operated by the European Southern Observatory (ESO) at La Silla, Chile, and on the 2.1-m SPM telescope, operated by the UNAM at the Observatorio Astronómico at San Pedro Mártir Observatory in Baja California, Mexico. We also use NASA/ESA HST data, obtained at the Space Telescope Science Institute.

REFERENCES

- Acker A., Raytchev B., Stenholm B., Tylenda R., 1991, *A&AS*, 90, 89
- Acker A., Marcout J., Ochsenbein F., Stenholm B., Tylenda R., Schohn C., 1992, *The Strasbourg-ESO Catalogue of Galactic Planetary Nebulae. Parts I, II.*
- Aleman I., Gruenwald R., 2011, *A&A*, 528A, 74

- Balick B., Preston H. L., Icke V., 1987, *AJ*, 94, 1641
- Balick B., Rugers M., Terzian Y., Chengalur J. N. 1993, *ApJ*, 411, 778
- Balick B., Perinotto M., Maccioni A., Terzian Y., Hajian A. R., 1994, *ApJ*, 424, 800
- Balick B., Alexander J., Hajian A. R., Terzian Y., Perinotto M., Patriarchi P., 1998, *AJ*, 116, 360
- Balick B., Frank A., 2002, *ARA&A*, 40, 439
- Blackman E. G., Frank A., Welch C., 2001, *ApJ*, 546, 288
- Boffin H. M. J., Miszalski B., Rauch T., Jones D., Corradi R. L. M., Napiwotski R., Day-Jones A. C., Koppen J., 2012, *Science*, 338, 773.
- Bohigas J., 2001, *RMxAA*, 37, 237
- Boumis P., Paleologou E. V., Mavromatakis F., Papamastorakis J., 2003, *MNRAS*, 339, 735
- Boumis P., Akras S., Xilouris E. M., Mavromatakis F., Kapakos E., Papamastorakis J., Goudis C. D., 2006, *MNRAS*, 367, 1551
- Cahn J. H., Kaler J. B., Stanghellini L., 1992, *A&AS*, 94, 399
- Corradi R. L. M., Manso R., Mampaso A., Schwarz H. E., 1996, *A&A*, 313, 913
- Corradi R. L. M., Perinotto M., Villaver E., Mampaso A., Gonçalves D., 1999, *AJ*, 523, 721
- Corradi R. L. M. García-Rojas J., Jones D., Rodríguez-Gil P., 2015, *ApJ*, 807, 99
- Delgado-Inglada G., Rodríguez M., Peimbert M., Stasińska, G., Morisset C., 2015, *MNRAS*, 449, 1797
- Dopita M. A., Sutherland R. S., 1996, *ApJS*, 102, 161
- Dopita M. A., 1997, *ApJ*, 485, L41
- De Marco O., 2009, *PASP*, 121, 316
- Exter K. M., Pollacco D. L., Bell S. A., 2003, *MNRAS*, 341, 1349
- Fitzpatrick E.L., 1999, *PASP*, 111, 63
- Frew D. J., Bojičić I. S., Parker Q. A., 2013, *MNRAS*, 431, 2
- García-Rojas J., Peña M., Morisset C., Delgado-Inglada G., Mesa-Delgado A., Ruiz T. M., 2013, 2013, *A&A*, 558A, 122
- García-Segura, G., Langer, N., Różyńska, M., Franco J., 1999, *ApJ*, 517, 767
- García-Segura G., Villaver E., Langer N., Yoon S.-C., Manchado A., 2014, *AJ*, 783, 74
- Gonçalves D. R., Corradi R. L. M., Mampaso A., 2001, *ApJ*, 547, 302
- Gonçalves D. R., Corradi R. L. M., Mampaso A., Perinotto M., 2003, *ApJ*, 597, 975
- Gonçalves D. R., 2004, *ASP Conference Proceedings*, 313, 216
- Gonçalves D. R., Mampaso A., Corradi R. L. M., Perinotto M., Riera A., López-Martín, 2004, *MNRAS*, 355, 37
- Gonçalves D. R., Ercolano B., Carnero A., Mampaso A., Corradi R. L. M., 2006, *MNRAS*, 365, 1039
- Gonçalves D. R., Mampaso A., Corradi R. L. M., Quireza C., 2009, *MNRAS*, 398, 2166-2176
- Górny S. K., Schwarz H. E., Corradi R. L. M., van Winckel H. 1999, *A&AS*, 136, 145
- Górny S. K., Chiappini C., Stasińska G., Cuisinier F., 2009, *A&A*, 500, 1089
- Guerrero M. A., Miranda L. F., Manchado A., Vázquez R., 2000, *MNRAS*, 313, 1
- Guerrero M. A., Toalá J. A., Medina J. J., Luridiana V., Miranda L. F., Riera A., Velázquez P. F., 2013, *A&A*, 557A, 121
- Guerrero M. A., De Marco O., 2013, *A&A*, 553A, 126
- Jones D., Santander-García M., Boffin H. M. J., Miszalski B., Corradi R. L. M., 2014, in *Asymmetrical Planetary Nebulae VI Conference*, 43.
- Henry R. B. C., Kwitter K. B., Balick B., 2004, *AJ*, 127, 2284
- Hora J. L., Hoffmann W. F., Deutsch L. K., Fazio G. G., 1990, *ApJ*, 353, 549
- Kingsburgh R. L., Barlow M. J., 1994, *MNRAS*, 271, 257
- Kaler J. B., 1970, *ApJ*, 160, 887
- Kwitter K. B., Henry R. B. C., 2001, *ApJ*, 562, 804
- Kwok, S., Purton, C. R., Fitzgerald, P. M. 1978, *ApJ*, 219, L125
- Leal-Ferreira M. L., Gonçalves D. R., Monteiro H., Richards J. W., 2011, *MNRAS*, 411, 1395
- Liu Y., Liu X.-W., Luo S.-G., Barlow M. J., 2004, *MNRAS*, 353, 1231
- Liu X.-W., Storey P. J., Barlow M. J., Danziger I. J., Cohen M., Bryce M., 2000, *MNRAS*, 312, 585.
- López J. A., Vázquez R., Rodríguez L. F., 1995, *ApJ*, 455, L63
- López J. A., Richer M. G., García-Díaz Ma. T., Clark D. M., Meaburn J., Riesgo H., Steffen W., Lloyd, M., 2012, *RevMexAA*, 48, 3
- Manchado A., Stanghellini L., Villaver E., García-Segura G., Shaw R. A., García-Hernández D. A., 2015, *ApJ*, 808, 115
- Manchado, A., Guerrero, M. A., Stanghellini, L., Serran-Ricart, M. 1996, *The IAC Morphological Catalog of Northern Galactic PNs (La Laguna : IAC)*
- Marcolino W. L. F., de Araújo F. X., 2003, *AJ*, 126, 887
- Marcolino W. L. F., de Araújo F. X., Junior H. B. M., Duarte E. S., 2007, *AJ*, 134, 1380
- McCarthy J. K. M Mould J. R., Mendez R. H., Kudritzki R. P., Husfeld D., Herrero A., Groth H. G., 1990, *ApJ*, 351, 230
- Meaburn J., Walsh J. R., Clegg R. E. S., Walton N. A., Taylor D., Berry D. S., 1992, *MNRAS*, 255, 177
- Mellema G., Eulderink F., Icke V. 1991, *A&A*, 252, 718
- Mellema G., 1995, *MNRAS*, 277, 173
- Mellema G., Raga A. C., Canto J., Lundqvist P., Balick B., Steffen W., Noriega-Crespo, A., 1998, *A&A*, 331, 335
- Mellema G., 2004, *A&A*, 416, 623
- Mendez R. H., Herrero A., Manchado A., 1990, *A&A*, 229, 152
- Mendez R. H., Kudritzki R. P., Herrero A., 1992, *A&A*, 260, 329
- Mendez R. H., Kudritzki R. P., Herrero, A., Husfeld D., Groth H. G., 1988, *A&A*, 190, 113
- Miranda L. F., Vázquez R., Corradi R. L. M., Guerrero M., A.; López J. A., Torrelles J. M., 1999, *ApJ*, 520, 714
- Miranda L. F., Guerrero M. A., Torrelles J. M., 2001, *MNRAS*, 322, 195
- Miszalski B., Acker A., Parker Q. A., Moffat A. F. J, 2009a, *A&A*, 505, 249
- Miszalski B., Acker A., Moffat A. F. J., Parker Q. A., Udalski A., 2009b, *A&A*, 496, 813
- Miszalski B., Jones D., Rodríguez-Gil P., Boffin H. M. J., Corradi R. L. M., Santander-García M. 2011, *A&A*, 531, 158

- Monteiro H., Gonçalves D. R., Leal-Ferreira M. L., Corradi R. L. M., 2013, *A&A*, 560, 102
- Nordhaus J., Blackman, E. G., 2006, *MNRAS*, 370, 2004
- ODell C. R., Handron K. D., 1996, *AJ*, 111, 1630
- Palen S., Balick B., Hajian A. R., Terzian Y., Bond H., E., Panagia N., 2002, *AJ*, 123, 2666
- Parker Q. A., Acker A., Frew, D. J., et al., 2006, *MNRAS*, 373, 79
- Parthasarathy M., Acker A., Stenholm B., 1998, *A&A*, 329L, 9
- Pereyra M., Richer M. G., López J. A., 2013, *ApJ*, 771, 114
- Perinotto M., 2000, *Ap&SS*, 274, 205
- Perinotto M., Morbidelli L., Scatarzi A., 2004, *MNRAS*, 349, 793
- Phillips, J. P., 2004, *MNRAS*, 353, 589
- Phillips, J. P., 2005, *MNRAS*, 362, 847
- Raga A. C., Riera A., Mellema G., Esquivel A., Velázquez P. F., 2008, *A&A*, 489, 1141
- Rauch T., Werner K. 1997, in *The Third Conference on Faint Blue Stars*, ed. A. G. D. Philip, J. Liebert, R. A. Saffer (Schenectady, NY: L.Davis Press), 217
- Riesgo H., López J. A., 2006, *RMxAA*, 42, 47
- Sabbadin F., Minello S., Bianchini A. 1977, *A&A*, 60, 147
- Sabin L., Parker Q. A., Corradi R. L. M., et al. 2014, 2014, *MNRAS*, 443, 3388
- Sahai R., Morris M. R., Villar G. G., 2011, *AJ*, 141, 134
- Schwarz H. E., Corradi R. L. M., Stanghellini L. 1993, in *IAU Symp. 155, Planetary Nebulae*, ed. R. Weinberger & A. Acker (Dordrecht: Kluwer), 214
- Shaw R. A., Kaler J. B., 1989, *ApJS*, 69, 495
- Shaw R. A., Dufour R. J., 1995, *PASP*, 107, 896
- Shaw R. A. 2012, in *IAU Symp. 283, Planetary Nebulae: An Eye to the Future*, ed. Manchado A., Stanghellini L., Sch onberner D., (Cambridge:Cambridge Univ. Press), 156
- Soker N., Livio M., 1994, *ApJ*, 421, 219
- Steffen W., López J. A., Lim A., 2001, *ApJ*, 556, 823
- Tocknell J., De Marco O., Wardle M., 2014, *MNRAS*, 439, 2014
- Tylenda R., Acker A., Stenholm B., Koepfen J., 1992, *A&AS*, 95, 337
- Tylenda R., Acker A., Stenholm B., 1993, *A&AS*, 102, 595
- Wang W., Liu X.-W., Zhang Y., Barlow M. J., 2004, *A&A*, 427, 873
- Wesson R., Liu X.-W., Barlow M. J., 2005, *MNRAS*, 362, 424

Table 2. IC 4846

Line ID	Inner NEB 3.5''(5) ^a	NE jet 2.1''(3)	SW jet 2.1''(3)	Entire NEB 10''(15)
[O II] 3727	20.45	100.2	116.5	26.78
H12 3750	2.421	—	—	2.682
H11 3770	2.994	—	—	3.364
H10 3798	4.415	—	—	4.723
He I 3819	0.933	—	—	1.216
H9 3835	5.792	—	—	6.461
[Ne III] 3869	66.91	84.11	102.9	76.43
[Ne III] + H I 3968	36.53	40.65	56.82	40.52
He I 4026	2.086	2.986	3.812	2.403
[S II] 4070	1.553	3.014	2.191	1.655
Hδ 4101	24.41	29.33	32.56	27.51
Hγ 4340	46.83	50.58	52.54	52.34
[O III] 4363	7.274	7.952	7.768	7.866
He I 4471	4.152	6.811	6.203	4.885
He II 4686	0.461	—	—	0.526
He I 4712 ^α	0.606	—	0.905	0.713
[Ar IV] 4712	1.035	—	3.026	1.111
[Ar IV] 4740	1.349	—	2.587	1.453
Hβ 4861	100.0	100.0	100.0	100.0
He I 4924	1.198	—	—	1.267
[O III] 4958	378.2	349.5	337.5	421.1
[O III] 5007	1150	1116	982.9	1257
[N I] 5200	0.173	—	—	0.201
[Fe III] 5270	0.129	—	—	0.174
[Cl III] 5517	0.333	0.852	1.328	0.377
[Cl III] 5537	0.466	0.771	1.227	0.546
[N II] 5755	0.425	1.282	1.089	0.459
He I 5876	14.19	15.59	14.14	14.18
[K IV] 6101	0.093	—	—	0.108
[O I] 6300	1.676	6.549	5.691	1.993
[S III] 6312	1.141	1.512	1.646	1.228
[O I] 6363	0.582	2.178	2.238	0.664
[N II] 6548	5.159	20.79	17.59	6.487
Hα 6564	285.0	285.0	285.0	285.0
[N II] 6584	16.54	51.45	45.97	19.13
He I 6678	3.142	3.546	3.769	3.089
[S II] 6716	1.128	5.433	4.996	1.378
[S II] 6731	2.069	7.506	7.052	2.579
log[F(Hβ) c(Hβ)]	-11.62 0.48±0.03	-13.49 0.50±0.05	-13.45 0.53±0.05	-11.54 0.52±0.03
Line Fluxes	Percentage errors in line fluxes			
(0.001-0.01)F _{Hβ}	13	43	43	12
(0.01-0.05)F _{Hβ}	10	27	26	10
(0.05-0.15)F _{Hβ}	9	12	12	8
(0.15-0.30)F _{Hβ}	8	10	10	7
(0.30-2.0)F _{Hβ}	7	9	9	7
(2.0-5.0)F _{Hβ}	7	8	7	7
(5.0-10.0)F _{Hβ}	6	7	7	6
> 10 F _{Hβ}	6	7	7	6
Electron Densities (cm ⁻³) and Temperatures (K)				
N _e [S II]	7200±1050	2150±400	2350±450	8050±1050
N _e [Ar IV]	8550±1400	—	2200±800	9100±1500
N _e [Cl III]	7400±1350	1650±950	1850±700	8050±1500
T _e [O III]	9900±1400	10350±1800	11100±1950	9850±1400
T _e [N II]	11950±2250	12800±4150	12450±4000	11400±2150
T _e [S II]	12700±2000	13700±4300	13250±4150	9500±1550

^a The size of the component in arcsec. The number of pixels used to extract the spectra is indicated in the parentheses for each component.

Table 3. Ionic and total abundances of IC 4846

Ionic abundances	T _e & N _e ^a	Inner NEB	NE jet	SW jet	Entire NEB
He ⁺ /H ⁺	1	0.077±0.009	0.091±0.014	0.088±0.013	0.078±0.009
He ⁺⁺ /H ⁺	2	0.0004±0.0001	—	—	0.0004±0.0001
ICF(He)		1.00	1.00	1.00	1.00
He/H		0.077±0.009	0.091±0.014	0.088±0.013	0.078±0.009
10 ⁵ × O ⁺ /H ⁺	1	0.78±0.08	2.07±0.28	2.55±0.33	1.31±0.13
10 ⁵ × O ²⁺ /H ⁺	2	40.7±3.8	34.4±3.9	23.9±2.8	45.4±4.2
ICF(O)		1.01±0.01	1.00	1.00	1.01±0.01
10 ⁴ × O/H		4.16±0.40	3.65±0.42	2.65±0.31	4.69±0.43
10 ⁵ × N ⁺ /H ⁺	1	0.22±0.03	0.61±0.08	0.56±0.07	0.29±0.03
ICF(N)		53.3±7.6	17.6±3.1	10.4±1.8	35.8±4.9
10 ⁴ × N/H		1.17±0.24	1.06±0.24	0.58±0.13	1.04±0.18
10 ⁶ × S ⁺ /H ⁺	1	0.12±0.02	0.25±0.07	0.24±0.07	0.16±0.02
10 ⁶ × S ²⁺ /H ⁺	2	2.75±0.26	3.18±0.97	2.53±0.71	2.98±0.36
ICF(S)		2.63±0.12	1.84±0.10	1.56±0.08	2.31±0.10
10 ⁶ × S/H		7.53±0.82	6.31±1.95	4.33±1.24	7.24±0.93
10 ⁸ × Cl ²⁺ /H ⁺	2	6.11±0.86	10.1±4.3	10.1±3.8	7.25±1.07
ICF(Cl)		2.74±0.40	1.98±0.86	1.71±0.69	2.43±0.43
10 ⁷ × Cl/H		1.68±0.34	2.00±1.22	1.73±0.95	1.76±0.41
10 ⁷ × Ar ³⁺ /H ⁺	2	2.35±0.33	—	3.75±1.16	2.55±0.35
ICF(Ar)		1.02±0.20	1.06±0.26	1.11±0.27	1.03±0.20
10 ⁷ × Ar/H		2.40±0.59	—	4.15±1.64	2.63±0.57
10 ⁵ × Ne ²⁺ /H ⁺	2	7.03±0.69	7.51±0.96	6.89±0.88	8.14±0.81
ICF(Ne)		1.02±0.14	1.06±0.17	1.11±0.18	1.03±0.14
10 ⁵ × Ne/H		7.19±1.21	7.96±1.65	7.62±1.59	8.40±1.38

^a 1: T_e[N II] and N_e[S II], 2: T_e[O III] and N_e[S II]

Table 4. Wray 17-1 (PA=155°)

Line ID	NW filament 11.6''(29)	NW knot 4.4''(11)	NW inner NEB 11.6''(29)	SE filament 10.8''(27)	SE knot 3.6''(9)	SE inner NEB 11.6''(29)
[O II] 3727	611.3	364.2	—	636.1	309.3	—
[Ne III] 3869	137.7	107.7	—	160.8	112.5	—
[Ne III] + H I 3968	54.22	—	—	65.39	43.71	—
H δ 4101	25.57	—	—	25.57	—	—
H γ 4340	46.09	48.56	45.31	49.85	—	44.21
[O III] 4363	14.18	10.48	6.044	16.37	—	8.292
He I 4471	2.666	—	—	1.587	—	—
He II 4686	53.93	66.46	113.6	60.58	63.21	112.8
[Ar IV]+He I 4712	2.795	—	4.921	2.456	—	4.056
[Ar IV] 4712	2.516	—	—	2.289	—	—
[Ar IV] 4740	1.817	—	3.505	1.659	—	2.845
H β 4861	100.0	100.0	100.0	100.0	100.0	100.0
He I 4924	1.009	—	—	1.016	—	—
[O III] 4958	405.3	298.4	118.1	466.5	393.4	154.9
[O III] 5007	1174	927.9	354.1	1369	1191	470.2
[N II] 5200	6.388	—	—	5.296	—	—
He II 5411	4.601	—	—	3.846	—	—
[N II] 5755	7.042	—	—	6.536	—	—
He I 5876	9.481	—	—	9.357	—	—
[O I] 6300	40.43	63.24	—	32.23	43.38	—
[O I] 6363	14.66	17.32	—	10.34	18.43	—
[N II] 6548	112.8	78.61	—	92.77	—	—
H α 6564	285.0	285.0	285.0	285.0	285.0	285.0
[N II] 6584	358.1	241.8	—	300.9	119.8	—
He I 6678	2.545	—	—	3.031	—	—
[S II] 6716	17.82	6.849	—	15.01	—	—
[S II] 6731	15.71	5.911	—	12.89	—	—
He I 7065	2.884	—	—	2.493	—	—
[Ar III] 7135	24.26	19.71	—	24.64	19.88	—
[O II] 7330	24.11	—	—	—	—	—
[Ar III] 7752	3.396	—	—	4.081	—	—
log[F(H β)]	-13.52	-15.05	-14.51	-13.52	-15.22	-14.26
c(H β)	0.09 \pm 0.03	0.10 \pm 0.08	0.06 \pm 0.05	0.11 \pm 0.04	0.12 \pm 0.09	0.07 \pm 0.06
Line Fluxes			Percentage errors in line fluxes			
(0.01-0.05)F _{Hβ}	26	—	45	25	—	44
(0.05-0.15)F _{Hβ}	18	43	36	17	45	33
(0.15-0.30)F _{Hβ}	12	31	26	12	35	22
(0.30-2.0)F _{Hβ}	8	18	15	9	20	15
(2.0-5.0)F _{Hβ}	7	16	12	8	17	11
(5.0-10.0)F _{Hβ}	6	14	—	6	15	—
> 10 F _{Hβ}	6	—	—	6	12	—
Electron Densities (cm ⁻³) and Temperatures (K)						
N _e [S II]	350 \pm 70	300 \pm 180	—	306 \pm 70	—	—
N _e [Ar IV]	300 \pm 110	—	160 \pm 110 ^a	325 \pm 115	—	100 \pm 60 ^a
T _e [O III]	12400 \pm 2560	12100 \pm 5490	14250 \pm 5460	12370 \pm 2460	—	14471 \pm 5250
T _e [N II]	11750 \pm 2350	—	—	12360 \pm 2110	—	—

^a N_e[Ar IV] is considered as a lower limit since the contribution of He I 4712 has not been subtracted.

Table 5. Ionic and total abundances of Wray 17-1 (PA=155°)

Ionic abundances	T _e & N _e ^a	NW filament	NW knot	NW inner NEB	SE filament	SE knot ^b	SE inner NEB
He ⁺ /H ⁺	1	0.068 \pm 0.014	—	—	0.071 \pm 0.014	—	—
He ⁺⁺ /H ⁺	2	0.046 \pm 0.005	0.056 \pm 0.013	0.098 \pm 0.02	0.047 \pm 0.006	0.053 \pm 0.015	0.097 \pm 0.021
ICF(He)		1.000	1.000	1.000	1.000	1.000	1.000
He/H		0.114 \pm 0.019	0.056 \pm 0.013	0.098 \pm 0.02	0.118 \pm 0.020	0.053 \pm 0.015	0.097
10 ⁵ \times O ⁺ /H ⁺	1	12.5 \pm 1.3	6.61 \pm 1.61	—	11.6 \pm 1.3	5.98 \pm 1.57	—
10 ⁵ \times O ²⁺ /H ⁺	2	20.7 \pm 2.1	17.7 \pm 4.1	4.21 \pm 0.82	24.2 \pm 2.6	23.4 \pm 5.6	5.35 \pm 0.99
ICF(O)		1.41 \pm 0.09	—	—	1.40 \pm 0.09	—	1.00
10 ⁴ \times O/H		4.68 \pm 0.55	>2.43 \pm 0.81	>0.42 \pm 0.82	5.02 \pm 0.63	>2.93 \pm 1.04	0.54 \pm 0.99
10 ⁵ \times N ⁺ /H ⁺	1	4.53 \pm 0.48	2.88 \pm 0.71	—	3.49 \pm 0.42	1.48 \pm 0.42	—
ICF(N)		3.76 \pm 0.58	—	—	4.33 \pm 0.72	—	—
10 ⁴ \times N/H		1.70 \pm 0.32	>0.29 \pm 0.07	—	1.51 \pm 0.31	>0.15 \pm 0.04	—
10 ⁶ \times S ⁺ /H ⁺	1	0.56 \pm 0.09	0.20 \pm 0.10	—	0.41 \pm 0.07	—	—
10 ⁶ \times S ²⁺ /H ⁺	2	3.01 \pm 0.48 ^c	—	—	2.13 \pm 0.38 ^c	—	—
ICF(S)		1.18 \pm 0.05	—	—	1.22 \pm 0.05	—	—
10 ⁶ \times S/H		4.23 \pm 0.68	>0.20 \pm 0.10	—	3.21 \pm 0.57	—	—
10 ⁷ \times Ar ²⁺ /H ⁺	1	12.8 \pm 1.9	11.8 \pm 4.2	—	12.1 \pm 1.8	12.3 \pm 4.9	—
10 ⁷ \times Ar ³⁺ /H ⁺	2	2.12 \pm 0.58	—	2.94 \pm 1.39	1.95 \pm 0.52	—	2.33 \pm 1.08
ICF(Ar)		1.36 \pm 0.11	—	—	1.30 \pm 0.09	—	—
10 ⁶ \times Ar/H		2.04 \pm 0.38	>1.18 \pm 0.42	>0.29 \pm 0.14	1.83 \pm 0.33	>1.23 \pm 0.50	>0.23 \pm 0.11
10 ⁵ \times Ne ²⁺ /H ⁺	2	6.17 \pm 0.69	5.28 \pm 1.34	—	7.28 \pm 0.93	5.86 \pm 1.18	—
ICF(Ne)		2.26 \pm 0.35	—	—	2.07 \pm 0.34	—	—
10 ⁴ \times Ne/H		1.39 \pm 0.27	>0.53 \pm 0.13	—	1.51 \pm 0.32	>0.59 \pm 0.12	—

^a 1: T_e[N II] and N_e[S II], 2: T_e[O III] and N_e[N II]

^b T_e and N_e are drawn from the NW knot.

^c It is calculated by using the equation S²⁺=S⁺*(4.677+(O²⁺/O)^{0.433}) from Kingsburgh & Barlow (1994).

Table 6. Wray 17-1 (PA=75°)

Line ID	E knot 2.8''(7)	E arc 14.8''(37)	E inner NEB 11.6''(29)	W knot 3.6''(9)	W arc 6''(15)	W inner NEB 11.6''(29)
[O II] 3727	237.4	57.55	—	253.3	38.46	—
[Ne III] 3869	66.42	52.69	—	113.9	58.18	—
[Ne III] + H γ 3968	28.35	31.61	—	47.23	21.86	—
H δ 4101	24.98	22.07	—	26.67	23.69	—
H γ 4340	46.89	46.45	44.89	45.39	47.89	48.79
[O III] 4363	9.577	9.244	—	9.039	12.83	4.863
He II 4686	92.72	106.1	103.8	96.99	100.1	113.6
[Ar IV]+He I 4712	6.617	6.087	9.894	7.862	8.816	10.53
[Ar IV] 4712	6.351	—	—	7.691	—	8.671
[Ar IV] 4740	4.597	4.366	7.071	5.668	6.238	7.414
H β 4861	100.0	100.0	100.0	100.0	100.0	100.0
He I 4924	—	—	—	5.043	—	—
[O III] 4958	180.9	281.5	85.08	250.2	308.9	86.51
[O III] 5007	533.1	843.8	259.2	762.5	937.1	263.1
[N I] 5200	4.978	—	—	2.563	—	—
He II 5411	9.557	8.051	—	7.658	11.34	3.934
[N II] 5755	3.842	—	—	3.621	—	—
He I 5876	6.556	—	—	3.958	3.409	—
[O I] 6300	37.13	—	—	24.06	—	—
[S III] 6312	—	—	—	2.541	—	—
[O I] 6363	11.05	—	—	6.103	—	—
[N II] 6548	60.38	8.051	—	49.81	7.555	—
H α 6564	285.0	285.0	285.0	285.0	285.0	285.0
[N II] 6584	183.2	21.82	—	159.5	26.55	4.999
He I 6678	—	—	—	—	2.094	—
[S II] 6716	4.986	—	—	11.91	5.129	—
[S II] 6731	4.435	—	—	12.36	4.083	—
[Ar V] 7005	5.591	—	7.921	—	—	7.619
[Ar III] 7135	12.29	12.58	—	15.42	15.99	3.479
[O II] 7330	—	—	—	5.383	—	—
log[F(H β)]	-14.85	-14.36	-14.49	-14.51	-14.41	-14.29
c(H β)	0.13 \pm 0.10	0.09 \pm 0.07	0.09 \pm 0.07	0.11 \pm 0.06	0.06 \pm 0.05	0.04 \pm 0.04
Line Fluxes						
(0.01-0.05)F $_{H\beta}$	43	38	—	37	36	36
(0.05-0.15)F $_{H\beta}$	36	31	34	30	28	30
(0.15-0.30)F $_{H\beta}$	26	26	26	20	19	23
(0.30-2.0)F $_{H\beta}$	17	14	14	12	11	14
(2.0-5.0)F $_{H\beta}$	14	10	11	9	9	11
(5.0-10.0)F $_{H\beta}$	10	9	—	8	8	—
Electron Densities (cm $^{-3}$) and Temperatures (K)						
N $_e$ [S II]	375 \pm 230	—	—	760 \pm 320	175 \pm 80	—
N $_e$ [Ar IV]	325 \pm 200	220 \pm 110 ^a	170 \pm 85 ^a	515 \pm 220	260 \pm 100	100 \pm 45 ^a
T $_e$ [O III]	14590 \pm 5550	12180 \pm 4025	—	12300 \pm 3920	13030 \pm 3920	14700 \pm 5600
T $_e$ [N II]	12130 \pm 5600	—	—	12420 \pm 4880	—	—

^a N $_e$ [Ar IV] is considered as a lower limit since the contribution of He I 4712 has not been subtracted.

Table 7. Ionic and total abundances of Wray 17-1 (PA=75°)

Ionic abundances	T $_e$ & N $_e^a$	E knot	E arc	E inner NEB ^b	W knot	W arc	W inner NEB
He $^+$ /H $^+$	1	0.047 \pm 0.020	—	—	0.029 \pm 0.011	0.032 \pm 0.012	—
He $^{++}$ /H $^+$	2	0.083 \pm 0.020	0.089 \pm 0.018	0.090 \pm 0.017	0.084 \pm 0.014	0.085 \pm 0.013	0.097 \pm 0.017
ICF(He)	—	1.000	1.000	1.000	1.000	1.000	1.000
He/H	—	0.130 \pm 0.040	0.089 \pm 0.018	0.090 \pm 0.017	0.113 \pm 0.025	0.117 \pm 0.025	0.097 \pm 0.017
10 5 \times O $^+$ /H $^+$	1	4.34 \pm 0.97	0.99 \pm 0.20	—	4.52 \pm 0.68	0.45 \pm 0.08	—
10 5 \times O $^{2+}$ /H $^+$	2	6.01 \pm 1.19	16.7 \pm 2.8	2.81 \pm 0.55	13.6 \pm 1.9	14.2 \pm 1.9	2.86 \pm 0.51
ICF(O)	—	1.97 \pm 0.41	—	—	2.47 \pm 0.51	2.37 \pm 0.47	—
10 4 \times O/H	—	2.04 \pm 0.60	>1.77 \pm 0.46	>0.28 \pm 0.06	4.47 \pm 1.13	3.47 \pm 0.83	>0.29 \pm 0.05
10 5 \times N $^+$ /H $^+$	1	2.19 \pm 0.53	0.26 \pm 0.08	—	1.73 \pm 0.31	0.23 \pm 0.07	0.04 \pm 0.02
ICF(N)	—	4.70 \pm 1.74	—	—	9.89 \pm 2.90	76.9 \pm 22.9	—
10 4 \times N/H	—	1.03 \pm 0.46	>0.03 \pm 0.01	—	1.71 \pm 0.59	1.77 \pm 0.75	>0.004 \pm 0.002
10 6 \times S $^+$ /H $^+$	1	0.16 \pm 0.08	—	—	0.38 \pm 0.12	0.12 \pm 0.05	—
10 6 \times S $^{2+}$ /H $^+$	2	0.84 \pm 0.41 ^c	—	—	2.71 \pm 1.06	0.64 \pm 0.27 ^c	—
ICF(S)	—	1.25 \pm 0.12	—	—	1.54 \pm 0.14	2.96 \pm 0.29	—
10 6 \times S/H	—	1.26 \pm 0.64	—	—	4.76 \pm 1.87	2.26 \pm 0.97	—
10 7 \times Ar $^{2+}$ /H $^+$	2	5.15 \pm 2.33	8.33 \pm 2.83	—	8.89 \pm 2.87	8.27 \pm 2.11	1.44 \pm 0.56
10 7 \times Ar $^{3+}$ /H $^+$	2	3.72 \pm 1.69	5.37 \pm 2.18	5.66 \pm 2.13	6.62 \pm 2.38	6.51 \pm 2.02	5.95 \pm 1.97
10 7 \times Ar $^{4+}$ /H $^+$	2	4.42 \pm 2.01	—	6.15 \pm 2.31	—	—	5.92 \pm 1.96
ICF(Ar)	—	1.27 \pm 0.17	—	—	1.11 \pm 0.05	1.01 \pm 0.07	—
10 6 \times Ar/H	—	1.69 \pm 0.80	>1.37 \pm 0.73	>1.28 \pm 0.68	>1.73 \pm 0.59	>1.50 \pm 0.42	>1.33 \pm 0.81
10 5 \times Ne $^{2+}$ /H $^+$	2	1.79 \pm 0.43	2.66 \pm 0.52	—	5.26 \pm 0.91	2.23 \pm 0.35	—
ICF(Ne)	—	3.39 \pm 1.21	—	—	3.30 \pm 0.96	2.45 \pm 0.67	—
10 4 \times Ne/H	—	0.61 \pm 0.26	>0.27 \pm 0.05	—	1.74 \pm 0.59	0.55 \pm 0.17	—

^a 1: T $_e$ [N II] and N $_e$ [S II], 2: T $_e$ [O III] and N $_e$ [N II]

^b T $_e$ is drawn from the W nebula

^c It is calculated by using the equation S $^{+2}$ =S $^{+}$ *(4.677+(O $^{+2}$ /O) $^{0.433}$) from Kingsburgh & Barlow (1994).

Table 8. K 1-2

Line ID	NW filament 7.6''(19)	NW knot 3.6''(9)	NW filament+Knot 11.6''(29)	SE knot 3.6''(9)	NW NEB 35.6''(89)
[O II] 3727	272.1	193.1	245.2	265.6	205.3
[Ne III] 3869	117.1	41.47	94.17	—	83.57
[Ne III] + H γ 3968	57.85	20.94	48.83	—	38.51
H δ 4101	23.63	26.61	24.31	—	23.93
H γ 4340	45.86	50.61	45.82	49.21	48.55
[O III] 4363	16.87	7.828	12.95	7.118	13.94
He II 4686	75.32	94.69	79.09	107.3	89.62
He I 4712 $^{\alpha}$	0.358	—	0.316	0.509	0.292
[Ar IV] 4712	6.544	8.405	8.430	9.265	7.599
[Ar IV] 4740	4.916	—	4.955	6.801	3.673
H β 4861	100.0	100.0	100.0	100.0	100.0
[O III] 4958	296.9	155.3	266.1	146.6	262.4
[O III] 5007	905.1	475.1	819.3	417.4	789.3
[N I] 5200	5.733	—	4.049	—	4.948
He II 5411	5.922	—	4.362	—	6.499
[N II] 5755	2.919	—	2.628	—	2.759
He I 5876	8.443	—	6.523	—	6.872
[O I] 6300	22.84	22.38	23.14	20.28	15.23
[S III] 6312	8.126	7.638	10.24	—	10.49
[O I] 6363	7.581	10.88	8.006	—	5.313
[N II] 6548	87.19	57.08	85.35	49.29	62.24
H α 6564	285.0	285.0	285.0	285.0	285.0
[N II] 6584	270.1	184.1	263.3	145.7	208.9
He I 6678	2.938	—	3.476	—	—
[S II] 6716	36.68	19.91	30.69	16.26	23.03
[S II] 6731	35.47	21.51	30.99	14.68	23.81
[Ar V] 7005	2.687	—	2.239	—	4.491
[Ar III] 7135	16.22	11.51	15.59	12.27	15.52
log[F(H β)]	-14.21	-14.87	-14.11	-15.01	-13.94
c(H β)	0.26 \pm 0.06	0.25 \pm 0.07	0.22 \pm 0.06	0.25 \pm 0.08	0.25 \pm 0.06
Line Fluxes	Percentage errors in line fluxes				
(0.01-0.05)F $_{H\beta}$	42	51	40	55	35
(0.05-0.15)F $_{H\beta}$	32	35	29	38	26
(0.15-0.30)F $_{H\beta}$	16	22	15	25	14
(0.30-2.0)F $_{H\beta}$	11	14	11	16	10
(2.0-5.0)F $_{H\beta}$	9	10	9	10	8
(5.0-10.0)F $_{H\beta}$	8	—	8	—	7
Electron Densities (cm $^{-3}$) and Temperatures (K)					
N $_e$ [S II]	520 \pm 80	888 \pm 280	610 \pm 100	422 \pm 150	700 \pm 140
N $_e$ [Ar IV]	755 \pm 340	—	—	492 \pm 260	—
T $_e$ [O III]	14820 \pm 2880	14010 \pm 5500	13800 \pm 4300	14250 \pm 5690	14470 \pm 2500
T $_e$ [N II]	9120 \pm 3950	—	8850 \pm 3700	—	9820 \pm 3600

Table 9. Ionic and total abundances of K 1-2

Ionic abundances	T $_e$ & N $_e^a$	NW filament	NW knot	NW filament+Knot	SE knot	NW NEB
He $^+$ /H $^+$	1	0.068 \pm 0.023	—	0.054 \pm 0.017	—	0.049 \pm 0.015
He $^{2+}$ /H $^+$	2	0.068 \pm 0.011	0.082 \pm 0.014	0.067 \pm 0.010	0.092 \pm 0.020	0.077 \pm 0.011
ICF(He)	—	1.000	1.00	1.000	1.000	1.000
He/H	—	0.136 \pm 0.034	0.082 \pm 0.014	0.121 \pm 0.027	0.092 \pm 0.020	0.126 \pm 0.026
10 5 \times O $^+$ /H $^+$	1	16.8 \pm 2.4	2.35 \pm 0.46	17.9 \pm 2.5	2.81 \pm 0.43	9.25 \pm 1.19
10 5 \times O $^{2+}$ /H $^+$	2	9.85 \pm 1.34	5.83 \pm 1.02	10.5 \pm 1.4	5.07 \pm 0.96	9.03 \pm 1.09
ICF(O)	—	1.59 \pm 0.20	—	1.71 \pm 0.22	—	1.88 \pm 0.26
10 4 \times O/H	—	4.23 \pm 0.79	> 0.82 \pm 0.16	4.86 \pm 0.92	>0.79 \pm 0.19	3.43 \pm 0.64
10 5 \times N $^+$ /H $^+$	1	6.64 \pm 1.08	1.63 \pm 0.28	7.07 \pm 1.01	1.25 \pm 0.28	4.11 \pm 0.55
ICF(N)	—	2.52 \pm 0.59	—	2.71 \pm 0.64	—	3.71 \pm 0.84
10 4 \times N/H	—	1.67 \pm 0.48	>0.16 \pm 0.03	1.92 \pm 0.53	>0.13 \pm 0.03	1.52 \pm 0.40
10 6 \times S $^+$ /H $^+$	1	2.28 \pm 0.41	0.53 \pm 0.15	2.16 \pm 0.36	—	1.26 \pm 0.22
10 6 \times S $^{2+}$ /H $^+$	2	4.59 \pm 1.55	5.18 \pm 1.95	6.48 \pm 1.94	—	4.21 \pm 1.26
ICF(S)	—	1.09 \pm 0.05	—	1.10 \pm 0.05	—	1.18 \pm 0.07
10 6 \times S/H	—	7.46 \pm 2.15	>5.71 \pm 1.26	9.52 \pm 2.57	—	6.45 \pm 1.78
10 7 \times Ar $^{2+}$ /H $^+$	2	6.59 \pm 1.49	5.21 \pm 1.96	7.24 \pm 2.11	5.38 \pm 2.21	6.61 \pm 1.98
10 7 \times Ar $^{3+}$ /H $^+$	2	3.78 \pm 1.56	5.54 \pm 2.61	5.08 \pm 1.97	5.76 \pm 2.37	3.71 \pm 1.23
10 7 \times Ar $^{4+}$ /H $^+$	2	2.05 \pm 0.86	—	2.01 \pm 0.83	—	3.61 \pm 1.37
ICF(Ar)	—	1.66 \pm 0.36	—	1.59 \pm 0.29	—	1.37 \pm 0.15
10 6 \times Ar/H	—	2.06 \pm 0.79	>1.08 \pm 0.65	2.27 \pm 0.88	>1.11 \pm 0.65	1.91 \pm 0.66
10 5 \times Ne $^{2+}$ /H $^+$	2	3.01 \pm 0.47	1.26 \pm 0.27	3.01 \pm 0.47	—	2.31 \pm 0.41
ICF(Ne)	—	4.30 \pm 0.99	—	4.64 \pm 1.08	—	3.80 \pm 0.84
10 4 \times Ne/H	—	1.29 \pm 0.48	>0.13 \pm 0.03	1.40 \pm 0.39	—	0.88 \pm 0.25

 a 1: T $_e$ [N II] and N $_e$ [S II], 2: T $_e$ [O III] and N $_e$ [S II]

Table 10. NGC 6891 (PA=135°)

Line ID	Inner NEB 4.9''(7)	NW knot 2.1''(3)	SE knot 2.1''(3)	NW outer NEB 4.9''(7)	SE outer NEB 4.9''(7)	Entire NEB 20.3''(29)
[O II] 3727	12.89	34.87	24.18	22.59	18.15	16.55
H12 3750	—	—	—	3.345	2.239	2.266
H11 3770	—	—	—	4.037	3.069	2.978
H10 3798	—	—	—	5.341	4.001	3.381
He I 3819	—	—	—	1.191	1.161	1.489
H9 3835	—	—	—	7.707	5.777	4.999
[Ne III] 3869	55.17	62.19	45.15	56.17	43.27	52.34
[Ne III] + H γ 3968	26.02	32.13	26.71	31.89	26.73	28.41
He I 4026	1.886	—	—	2.129	2.013	1.876
[S II] 4070	1.184	—	—	—	—	0.721
H δ 4101	22.21	24.81	26.64	24.92	24.69	23.55
H γ 4340	43.62	46.12	49.89	50.29	48.47	44.14
[O III] 4363	5.311	4.811	4.669	4.894	4.855	4.817
He I 4387	0.723	—	—	1.088	0.639	0.609
He I 4471	4.755	6.338	5.978	5.856	4.341	4.973
He II 4686	1.817	—	—	—	—	0.631
He I 4712 α	0.499	0.665	0.628	0.615	0.465	0.522
[Ar IV] 4712	0.625	—	—	0.455	0.508	0.597
[Ar IV] 4740	0.756	—	—	0.439	0.419	0.518
H β 4861	100.0	100.0	100.0	100.0	100.0	100.0
He I 4924	1.055	—	—	1.441	1.302	1.322
[O III] 4958	296.2	280.9	296.6	266.5	290.6	289.1
[O III] 5007	851.3	833.9	885.3	813.4	893.6	858.6
[Cl III] 5517	0.232	—	—	0.437	0.357	0.488
[Cl III] 5537	0.223	—	—	0.431	0.363	0.501
[N II] 5755	—	—	—	0.107	0.091	0.167
He I 5876	16.86	14.67	17.74	15.09	17.44	16.38
[S III] 6312	0.292	—	—	0.623	0.509	0.361
[N II] 6548	2.124	6.153	5.272	2.029	2.807	2.752
H α 6564	285.0	285.0	285.0	285.0	285.0	285.0
[N II] 6584	5.771	14.88	16.92	7.335	7.684	6.971
He I 6678	4.479	4.883	5.386	4.151	3.985	4.333
[S II] 6716	0.261	0.799	1.473	0.229	0.355	0.271
[S II] 6731	0.312	0.929	1.559	0.314	0.496	0.332
log[F(H β)]	-11.68	-13.58	-13.52	-12.14	-12.05	-11.29
c(H β)	0.03±0.02	0.03±0.03	0.03±0.03	0.06±0.04	0.05±0.03	0.05±0.03
Line Fluxes						
(0.001-0.01)F $_{H\beta}$	32	48	49	36	36	30
(0.01-0.05)F $_{H\beta}$	17	36	35	22	23	15
(0.05-0.15)F $_{H\beta}$	13	32	30	16	17	11
(0.15-0.30)F $_{H\beta}$	9	22	21	13	12	9
(0.30-2.0)F $_{H\beta}$	8	13	14	9	8	7
(2.0-5.0)F $_{H\beta}$	6	11	10	8	8	6
Electron Densities (cm $^{-3}$) and Temperatures (K)						
N $_e$ [S II]	1190±530	1150±670	750±440	1910±980	1980±1020	1420±600
N $_e$ [Ar IV]	7470±3400	—	—	3650±1860	1680±860	2260±960
N $_e$ [Cl III]	2180±980	—	—	2430±1240	2660±1360	2820±1200
T $_e$ [O III]	9930±1960	9700±3690	9460±3500	9820±2420	9530±2340	9600±1740
T $_e$ [N II]	—	—	—	10055±4130	9200±3790	12720±4230

Table 11. Ionic and total abundances of NGC 6891 (PA=135°)

Ionic abundances	T $_e$ & N $_e^a$	Inner NEB	NW knot	SE knot	NW outer NEB	SE outer NEB	Entire NEB
He $^+$ /H $^+$	1	0.116±0.018	0.104±0.040	0.129±0.050	0.103±0.016	0.114±0.018	0.107±0.015
He $^{++}$ /H $^+$	2	0.0015±0.0003	—	—	—	—	0.0005±0.0002
ICF(He)	—	1.000	1.000	1.000	1.000	1.000	1.000
He/H	—	0.118±0.018	0.104±0.040	0.129±0.050	0.103±0.016	0.114±0.018	0.108±0.015
10 5 × O $^+$ /H $^+$	1	0.59±0.09	1.79±0.54	1.32±0.41	1.09±0.18	1.34±0.21	0.31±0.05
10 5 × O $^{2+}$ /H $^+$	2	30.3±3.1	31.9±7.8	37.1±9.1	29.3±3.5	35.8±4.3	34.1±3.7
ICF(O)	—	1.01±0.00	1.00	1.00	1.00	1.00	1.00±0.00
10 4 × O/H	—	3.12±0.32	3.36±0.84	3.84±0.95	3.03±0.37	3.71±0.45	3.45±0.38
10 5 × N $^+$ /H $^+$	1	0.12±0.02	0.35±0.14	0.39±0.15	0.15±0.03	0.20±0.04	0.08±0.02
ICF(N)	—	53.8±9.7	18.8±7.4	29.1±11.6	27.8±5.7	27.7±8.1	111±22
10 4 × N/H	—	0.63±0.16	0.66±0.37	1.13±0.63	0.42±0.12	0.55±0.16	0.89±0.28
10 7 × S $^+$ /H $^+$	1	0.16±0.05	0.51±0.26	0.91±0.46	0.17±0.04	0.33±0.08	0.11±0.03
10 6 × S $^{2+}$ /H $^+$	2	0.71±0.24	0.29±0.15 ^b	0.52±0.26 ^b	1.59±0.61	1.49±0.56	1.02±0.32
ICF(S)	—	2.62±0.16	1.88±0.23	2.16±0.28	2.13±0.14	2.12±0.14	3.34±0.22
10 6 × S/H	—	1.90±0.65	0.64±0.33	1.31±0.68	3.42±1.33	3.23±1.22	3.45±1.03
10 8 × Cl $^{2+}$ /H $^+$	2	2.96±0.99	—	—	5.95±2.22	5.47±2.03	7.25±2.27
ICF(Cl)	—	2.68±1.29	2.21±1.62	2.54±1.85	2.15±1.17	2.17±1.16	3.38±0.15
10 8 × Cl/H	—	7.93±4.65	—	—	12.79±8.45	11.87±7.71	24.47±13.39
10 7 × Ar $^{3+}$ /H $^+$	2	1.29±0.43	—	—	0.86±0.33	0.97±0.35	1.15±0.38
ICF(Ar)	—	1.03±0.19	1.06±0.59	1.04±0.58	1.04±0.26	1.04±0.26	1.01±0.20
10 7 × Ar/H	—	1.33±0.51	—	—	0.89±0.41	1.01±0.44	1.16±0.45
10 5 × Ne $^{2+}$ /H $^+$	2	5.67±0.65	7.09±2.21	5.74±1.79	6.07±0.77	5.33±0.69	6.24±0.57
ICF(Ne)	—	1.03±0.15	1.06±0.37	1.04±0.36	1.04±0.18	1.04±0.18	1.01±0.16
10 5 × Ne/H	—	5.82±0.98	7.49±3.51	5.94±2.79	6.30±1.34	5.53±1.19	6.32±1.13

^a 1: T $_e$ [N II] and N $_e$ [S II], 2: T $_e$ [O III] and N $_e$ [S II].

^c It is calculated by using the equation S $^{+2}$ =S $^{+*}$ (4.677+(O $^{+2}$ /O) $^{0.433}$) from Kingsburgh & Barlow (1994).

Table 12. NGC 6891 (PA=45°)

Line ID	Inner NEB 4.9''(7)	NE NEB 6.3''(9)	SW NEB 6.3''(9)	Entire NEB 20.3''(29)
[O II] 3727	11.31	15.92	17.08	12.77
H12 3750	—	2.752	2.714	2.326
H11 3770	—	3.204	3.144	2.633
H10 3798	—	4.656	4.713	3.099
He I 3819	—	1.978	1.573	1.259
H9 3835	—	6.902	7.545	4.285
[Ne III] 3869	54.81	45.61	48.82	52.55
[Ne III] + H I 3968	24.85	27.59	28.06	27.19
He I 4026	1.698	2.389	2.206	2.004
[S II] 4070	—	—	—	0.474
Hδ 4101	22.84	24.89	24.07	22.98
Hγ 4340	42.87	46.56	43.87	45.32
[O III] 4363	4.931	4.152	3.698	4.682
He I 4387	0.591	0.909	0.731	0.399
He I 4471	5.176	5.317	4.309	5.045
He II 4686	1.994	—	—	0.855
He I 4712 ^α	0.543	0.558	0.452	0.529
[Ar IV] 4712	0.589	0.749	0.421	0.705
[Ar IV] 4740	0.699	—	0.399	0.645
Hβ 4861	100.0	100.0	100.0	100.0
He I 4924	1.263	1.515	1.061	1.253
[O III] 4958	289.3	279.5	265.6	302.3
[O III] 5007	889.9	849.5	780.7	872.6
[Cl III] 5517	0.211	0.407	0.411	0.529
[Cl III] 5537	0.198	0.379	0.397	0.518
[N II] 5755	—	—	—	0.158
He I 5876	16.94	17.36	15.05	16.57
[S III] 6312	0.235	0.338	0.538	0.311
[N II] 6548	2.393	2.923	2.512	2.848
Hα 6564	285.0	285.0	285.0	285.0
[N II] 6584	5.916	6.901	6.953	6.844
He I 6678	4.291	4.194	4.141	4.348
[S II] 6716	0.225	0.291	0.209	0.302
[S II] 6731	0.277	0.374	0.248	0.349
log[F(Hβ)]	-11.64	-12.31	-12.11	-11.31
c(Hβ)	0.05±0.03	0.04±0.03	0.05±0.03	0.04±0.03
Line Fluxes				
(0.001-0.01)F _{Hβ}	33	35	34	29
(0.01-0.05)F _{Hβ}	17	24	25	14
(0.05-0.15)F _{Hβ}	14	17	17	12
(0.15-0.30)F _{Hβ}	9	14	13	9
(0.30-2.0)F _{Hβ}	7	8	8	7
(2.0-5.0)F _{Hβ}	7	8	8	7
Electron Densities (cm ⁻³) and Temperatures (K)				
N _e [S II]	1300±610	1500±750	1110±530	1200±500
N _e [Ar IV]	7000±3270	—	3330±1600	2900±1190
N _e [Cl III]	1950±910	1920±960	2420±1160	2350±970
T _e [O III]	9590±1920	9250±2440	9200±2510	9500±1670
T _e [N II]	—	—	—	12190±3870

Table 13. Ionic and total abundances of NGC 6891 (PA=45°)

Ionic abundances	T _e & N _e ^a	Inner NEB	NE NEB	SW NEB	Entire NEB
He ⁺ /H ⁺	1	0.113±0.017	0.104±0.019	0.099±0.018	0.109±0.015
He ⁺⁺ /H ⁺	2	0.0016±0.0004	—	—	0.0007±0.0002
ICF(He)	—	1.000	1.000	1.000	1.000
He/H	—	0.115±0.017	0.104±0.019	0.099±0.018	0.110±0.015
10 ⁵ × O ⁺ /H ⁺	1	0.63±0.09	1.05±0.20	1.12±0.21	0.26±0.04
10 ⁵ × O ²⁺ /H ⁺	2	34.9±3.5	39.1±4.4	36.6±4.1	36.5±3.6
ICF(O)	—	1.01±0.00	1.00	1.00	1.00±0.00
10 ⁴ × O/H	—	3.58±0.36	4.02±0.46	3.77±0.44	3.70±0.37
10 ⁵ × N ⁺ /H ⁺	1	0.14±0.03	0.19±0.04	0.18±0.04	0.09±0.02
ICF(N)	—	56.9±9.9	38.3±8.5	33.7±7.4	142±26
10 ⁴ × N/H	—	0.80±0.22	0.73±0.22	0.61±0.19	1.28±0.37
10 ⁷ × S ⁺ /H ⁺	1	0.16±0.05	0.23±0.08	0.16±0.06	0.21±0.06
10 ⁶ × S ²⁺ /H ⁺	2	0.67±0.24	1.16±0.41	1.87±0.66	0.92±0.29
ICF(S)	—	2.68±0.15	2.36±0.17	2.26±0.16	3.63±0.22
10 ⁶ × S/H	—	1.84±0.67	2.79±1.01	4.27±1.54	3.41±1.09
10 ⁸ × Cl ²⁺ /H ⁺	2	2.99±1.03	6.58±2.31	6.71±2.34	7.89±2.35
ICF(Cl)	—	2.75±1.398	2.40±1.13	2.28±1.15	3.71±1.67
10 ⁸ × Cl/H	—	8.21±5.046	15.81±9.73	15.31±9.38	29.26±15.77
10 ⁷ × Ar ³⁺ /H ⁺	2	1.35±0.46	1.57±0.54	0.98±0.33	1.45±0.44
ICF(Ar)	—	1.03±0.21	1.03±0.23	1.03±0.24	1.01±0.20
10 ⁷ × Ar/H	—	1.39±0.55	1.61±0.66	1.01±0.41	1.47±0.53
10 ⁵ × Ne ²⁺ /H ⁺	2	6.56±0.65	6.56±0.74	7.03±0.80	6.56±0.65
ICF(Ne)	—	1.03±0.14	1.03±0.17	1.03±0.17	1.01±0.14
10 ⁵ × Ne/H	—	6.74±1.16	6.74±1.33	7.25±1.43	6.64±1.13

^a 1: T_e[N II] and N_e[S II], 2: T_e[O III] and N_e[S II]

Table 14. NGC 6572 (PA=160°)

Line ID	Inner NEB 7.7''(11)	N knot 2.1''(3)	S knot 2.1''(3)	Entire NEB 17.5''(25)
[O II] 3727	27.25	127.8	143.6	34.75
H12 3750	3.901	—	—	3.325
H11 3770	4.193	—	—	3.815
H10 3798	5.295	—	—	5.671
He I 3819	1.735	—	—	1.771
H9 3835	7.183	—	—	7.059
[Ne III] 3869	93.02	111.3	137.3	96.82
[Ne III] + H I 3968	45.14	54.09	72.41	46.21
He I 4026	2.562	—	—	2.739
[S II] 4070	2.537	—	—	2.754
Hδ 4101	23.95	24.43	28.53	26.42
Hγ 4340	46.22	44.51	45.26	47.79
[O III] 4363	9.183	7.143	9.579	9.651
He I 4387	0.805	—	—	0.823
He I 4471	5.541	6.701	7.006	5.827
He II 4686	1.014	—	—	0.906
He I 4712 ^α	0.808	0.978	1.022	0.851
[Ar IV] 4712	1.259	—	—	1.172
[Ar IV] 4740	2.761	—	—	2.607
Hβ 4861	100.0	100.0	100.0	100.0
He I 4924	1.475	—	—	1.355
[O III] 4958	383.2	372.9	441.9	418.8
[O III] 5007	1225	1122	1331	1243
[N I] 5200	0.274	5.733	—	0.348
[Cl III] 5517	0.239	—	—	0.268
[Cl III] 5537	0.538	—	—	0.602
[N II] 5755	2.136	4.921	3.665	2.337
He I 5876	18.34	17.98	18.79	18.27
[O I] 6300	5.225	11.96	17.97	5.963
[S III] 6312	1.174	—	—	1.201
[O I] 6363	1.684	4.483	6.707	1.841
[N II] 6548	18.41	67.85	54.21	19.81
Hα 6564	285.0	285.0	285.0	285.0
[N II] 6584	55.56	196.1	161.6	60.55
He I 6678	4.535	4.045	4.283	4.524
[S II] 6716	0.763	3.545	2.867	0.887
[S II] 6731	1.592	6.832	5.579	1.853
log[F(Hβ)]	-10.32	-12.49	-12.54	-10.26
c(Hβ)	0.27±0.01	0.25±0.05	0.29±0.06	0.27±0.02
Line Fluxes (0.001-0.01)F _{Hβ}	13	40	40	13
(0.01-0.05)F _{Hβ}	9	33	32	9
(0.05-0.15)F _{Hβ}	7	23	22	7
(0.15-0.30)F _{Hβ}	6	18	18	6
(0.30-2.0)F _{Hβ}	5	12	12	6
(2.0-5.0)F _{Hβ}	5	9	9	5
(5.0-10.0)F _{Hβ}	5	—	—	5
> 10 F _{Hβ}	5	6	6	5
Electron Densities (cm ⁻³) and Temperatures (K)				
N _e [S II]	21300±3370	9820±3900	10420±4200	21580±3400
N _e [Ar IV]	27000±3630	—	—	29300±3940
N _e [Cl III]	35230±6480	—	—	35200±6480
T _e [O III]	10200±1230	9900±2670	10260±2770	10200±1230
T _e [N II]	12350±1640	11350±3970	10730±3750	12220±1630
T _e [S II]	9100±1300	—	—	9820±1420

Table 15. Ionic and total abundances of NGC 6572 (PA=160°)

Ionic abundances	T _e & N _e ^a	Inner NEB	N knot	S knot	Entire NEB
He ⁺ /H ⁺	1	0.095±0.008	0.099±0.021	0.105±0.023	0.095±0.008
He ⁺⁺ /H ⁺	2	0.0008±0.0001	—	—	0.0008±0.0001
ICF(He)		1.00	1.00	1.0	1.00
He/H		0.096±0.008	0.099±0.021	0.105±0.029	0.096±0.008
10 ⁵ × O ⁺ /H ⁺	1	1.77±0.13	7.02±1.19	10.21±1.73	2.38±0.20
10 ⁵ × O ²⁺ /H ⁺	2	38.7±2.7	36.1±5.4	41.7±6.3	40.9±3.2
ICF(O)		1.01±0.11	1.00	1.00	1.01±0.11
10 ⁴ × O/H		4.07±0.54	4.31±0.66	5.20±0.80	4.35±0.59
10 ⁵ × N ⁺ /H ⁺	1	0.76±0.06	3.12±0.53	2.93±0.49	0.88±0.07
ICF(N)		23.0±3.5	6.14±1.40	5.09±1.16	18.3±2.9
10 ⁴ × N/H		1.75±0.30	1.915±0.55	1.49±0.42	1.608±2.88
10 ⁶ × S ⁺ /H ⁺	1	0.17±0.02	0.48±0.17	0.46±0.16	0.18±0.02
10 ⁶ × S ²⁺ /H ⁺	2	2.38±0.27	2.69±0.95 ^b	2.57±0.90 ^b	2.45±0.28
ICF(S)		2.00±0.10	1.34±0.09	1.28±0.08	1.86±0.09
10 ⁶ × S/H		5.10±0.63	4.25±1.53	3.87±1.37	4.89±0.61
10 ⁸ × Cl ²⁺ /H ⁺	3	6.74±0.94	—	—	7.57±1.08
ICF(Cl)		2.14±0.36	1.58±0.80	1.51±0.75	1.20±0.34
10 ⁸ × Cl/H		14.45±0.32	—	—	15.12±0.34
10 ⁷ × Ar ³⁺ /H ⁺	2	3.86±0.44	—	—	3.59±0.42
ICF(Ar)		1.05±0.19	1.20±0.39	1.25±0.40	1.06±0.20
10 ⁷ × Ar/H		4.06±0.87	—	—	3.82±0.86
10 ⁵ × Ne ²⁺ /H ⁺	2	8.58±0.61	8.27±1.41	12.31±2.11	8.93±0.69
ICF(Ne)		1.05±0.16	1.19±0.26	1.25±0.27	1.06±0.17
10 ⁵ × Ne/H		9.02±1.50	9.88±2.71	15.31±4.21	9.50±1.67

^a 1: T_e[N II] and N_e[S II], 2: T_e[O III] and N_e[Ar IV] and 3: T_e[O III] and N_e[Cl III].

^b It is calculated by using the equation S²⁺=S⁺*(4.677+(O²⁺/O)^{0.433}) from Kingsburgh & Barlow (1994).

Table 16. NGC 6572 (PA=15°)

Line ID	Inner NEB 7.7''(11)	N knot 2.1''(3)	S knot 2.1''(3)	Entire NEB 17.5''(25)
[O II] 3727	27.91	139.9	101.3	34.69
H12 3750	3.337	—	—	2.773
H11 3770	3.667	—	—	3.531
H10 3798	4.948	—	—	4.986
He I 3819	1.243	—	—	1.208
H9 3835	7.024	—	—	6.933
[Ne III] 3869	92.18	131.1	113.6	92.17
[Ne III] 3968	45.01	66.21	57.23	44.48
He I 4026	2.729	—	—	2.265
[S II] 4070	2.202	—	—	2.332
H δ 4101	25.75	24.73	26.06	25.45
H γ 4340	45.62	50.88	44.76	45.57
[O III] 4363	8.615	11.71	8.384	8.675
He I 4471	5.399	6.976	9.133	5.508
He II 4686	0.995	—	—	0.853
He I 4712 ^{α}	0.788	1.018	1.331	0.805
[Ar IV] 4712	1.169	—	—	1.011
[Ar IV] 4740	2.558	—	—	2.341
H β 4861	100.0	100.0	100.0	100.0
He I 4924	1.456	—	—	1.646
[O III] 4958	420.1	434.1	387.8	393.8
[O III] 5007	1229	1360	1104	1207
[N I] 5200	0.373	—	—	0.443
[Cl III] 5517	0.278	—	—	0.276
[Cl III] 5537	0.559	—	—	0.575
[N II] 5755	2.141	3.171	4.152	2.316
He I 5876	17.84	14.91	14.95	17.88
[O I] 6300	5.218	15.08	12.93	6.112
[S III] 6312	1.038	—	—	1.075
[O I] 6363	1.638	4.837	4.422	1.913
[N II] 6548	16.78	66.71	58.81	21.21
H α 6564	285.0	285.0	285.0	285.0
[N II] 6584	52.88	199.6	177.1	64.52
He I 6678	4.441	3.887	4.295	4.424
[S II] 6716	0.731	2.425	2.394	0.866
[S II] 6731	1.519	4.682	4.767	1.803
log[F(H β)]	-10.31	-12.24	-12.35	-10.23
c(H β)	0.29 \pm 0.02	0.29 \pm 0.06	0.24 \pm 0.05	0.28 \pm 0.01
Line Fluxes				
(0.001-0.01)F _{Hβ}	14	38	38	13
(0.01-0.05)F _{Hβ}	9	33	33	9
(0.05-0.15)F _{Hβ}	7	22	23	7
(0.15-0.30)F _{Hβ}	6	17	18	6
(0.30-2.0)F _{Hβ}	5	13	13	5
(2.0-5.0)F _{Hβ}	5	8	8	5
(5.0-10.0)F _{Hβ}	5	—	—	5
> 10 F _{Hβ}	5	6	6	5
Electron Densities (cm ⁻³) and Temperatures (K)				
N _e [S II]	20380 \pm 2600	9600 \pm 4480	12620 \pm 5900	20380 \pm 2600
N _e [Ar IV]	26380 \pm 3360	—	—	29650 \pm 3780
N _e [Cl III]	22750 \pm 4500	—	—	25930 \pm 5130
T _e [O III]	10000 \pm 1200	10890 \pm 2650	10400 \pm 2620	10050 \pm 1200
T _e [N II]	12780 \pm 1700	9420 \pm 3275	10570 \pm 3670	11925 \pm 1600
T _e [S II]	10360 \pm 1500	—	—	8990 \pm 1300

Table 17. Ionic and total abundances of NGC 6572 (PA=15°)

Ionic abundances	T _e & N _e ^a	Inner NEB	N knot	S knot	Entire NEB
He ⁺ /H ⁺	1	0.093 \pm 0.007	0.098 \pm 0.022	0.095 \pm 0.022	0.096 \pm 0.007
He ⁺⁺ /H ⁺	2	0.0009 \pm 0.0001	—	—	0.0007 \pm 0.0001
ICF(He)	1.00	1.00	1.00	1.00	1.00
He/H	0.094 \pm 0.007	0.098 \pm 0.022	0.095 \pm 0.022	0.097 \pm 0.007	0.097 \pm 0.007
10 ⁵ × O ⁺ /H ⁺	1	1.52 \pm 0.11	19.56 \pm 3.59	8.59 \pm 1.57	2.51 \pm 0.18
10 ⁵ × O ²⁺ /H ⁺	2	43.2 \pm 3.1	34.5 \pm 5.1	34.2 \pm 5.1	41.9 \pm 3.1
ICF(O)	1.01 \pm 0.10	1.00	1.00	1.00	1.01 \pm 0.10
10 ⁴ × O/H	4.51 \pm 0.52	5.41 \pm 0.87	4.28 \pm 0.66	4.47 \pm 0.54	4.47 \pm 0.54
10 ⁵ × N ⁺ /H ⁺	1	0.67 \pm 0.06	5.33 \pm 0.97	3.39 \pm 0.62	0.98 \pm 0.08
ICF(N)	29.6 \pm 4.2	2.77 \pm 0.68	4.99 \pm 1.19	17.8 \pm 2.5	17.8 \pm 2.5
10 ⁴ × N/H	1.99 \pm 0.33	1.47 \pm 0.45	1.69 \pm 0.51	1.75 \pm 0.28	1.75 \pm 0.28
10 ⁶ × S ⁺ /H ⁺	1	0.13 \pm 0.02	0.53 \pm 0.19	0.45 \pm 0.17	0.18 \pm 0.02
10 ⁶ × S ²⁺ /H ⁺	2	2.31 \pm 0.24	2.92 \pm 1.05 ^b	2.51 \pm 0.95 ^b	2.34 \pm 0.24
ICF(S)	2.17 \pm 0.11	1.11 \pm 0.05	1.27 \pm 0.08	1.85 \pm 0.08	1.85 \pm 0.08
10 ⁶ × S/H	5.30 \pm 0.62	3.81 \pm 1.38	5.43 \pm 1.44	4.65 \pm 0.52	4.65 \pm 0.52
10 ⁸ × Cl ²⁺ /H ⁺	3	7.71 \pm 1.15	—	—	7.67 \pm 1.07
ICF(Cl)	2.29 \pm 0.36	—	—	—	1.99 \pm 0.30
10 ⁸ × Cl/H	17.67 \pm 3.81	—	—	—	15.24 \pm 3.31
10 ⁷ × Ar ³⁺ /H ⁺	2	3.77 \pm 0.39	—	—	3.32 \pm 0.34
ICF(Ar)	1.04 \pm 0.18	—	—	—	1.07 \pm 0.18
10 ⁷ × Ar/H	3.93 \pm 0.79	—	—	—	3.54 \pm 0.71
10 ⁵ × Ne ²⁺ /H ⁺	2	9.19 \pm 0.65	10.03 \pm 1.84	6.72 \pm 1.24	9.02 \pm 0.64
ICF(Ne)	1.04 \pm 0.15	1.57 \pm 0.34	1.25 \pm 0.27	1.07 \pm 0.15	1.07 \pm 0.15
10 ⁵ × Ne/H	9.57 \pm 1.51	15.71 \pm 4.48	8.41 \pm 2.38	9.61 \pm 1.50	9.61 \pm 1.50

^a 1: T_e[N II] and N_e[S II], 2: T_e[O III] and N_e[Ar IV] and 3: T_e[O III] and N_e[Cl III].^b It is calculated by using the equation S²⁺=S⁺*(4.677+(O²⁺/O)^{0.433}) from Kingsburgh & Barlow (1994).